

R
086071

JPRS-CST-86-006

13 February 1986

China Report

SCIENCE AND TECHNOLOGY

19981020 104

[DTIC QUALITY INSPECTED 8]

FBIS

FOREIGN BROADCAST INFORMATION SERVICE

REPRODUCED BY
**NATIONAL TECHNICAL
INFORMATION SERVICE**
U.S. DEPARTMENT OF COMMERCE
SPRINGFIELD, VA. 22161

1
66
A64

NOTE

JPRS publications contain information primarily from foreign newspapers, periodicals and books, but also from news agency transmissions and broadcasts. Materials from foreign-language sources are translated; those from English-language sources are transcribed or reprinted, with the original phrasing and other characteristics retained.

Headlines, editorial reports, and material enclosed in brackets [] are supplied by JPRS. Processing indicators such as [Text] or [Excerpt] in the first line of each item, or following the last line of a brief, indicate how the original information was processed. Where no processing indicator is given, the information was summarized or extracted.

Unfamiliar names rendered phonetically or transliterated are enclosed in parentheses. Words or names preceded by a question mark and enclosed in parentheses were not clear in the original but have been supplied as appropriate in context. Other unattributed parenthetical notes within the body of an item originate with the source. Times within items are as given by source.

The contents of this publication in no way represent the policies, views or attitudes of the U.S. Government.

PROCUREMENT OF PUBLICATIONS

JPRS publications may be ordered from the National Technical Information Service, Springfield, Virginia 22161. In ordering, it is recommended that the JPRS number, title, date and author, if applicable, of publication be cited.

Current JPRS publications are announced in Government Reports Announcements issued semi-monthly by the National Technical Information Service, and are listed in the Monthly Catalog of U.S. Government Publications issued by the Superintendent of Documents, U.S. Government Printing Office, Washington, D.C. 20402.

Correspondence pertaining to matters other than procurement may be addressed to Joint Publications Research Service, 1000 North Glebe Road, Arlington, Virginia 22201.

7

13 February 1986

CHINA REPORT
SCIENCE AND TECHNOLOGY

CONTENTS

APPLIED SCIENCES

Specter of War in Space Discussed-Part II (Bao Xianmin; HANGTIAN, No 6, Nov 85).....	1
Lifetime of Excimer Laser Studied (Hu Xuejin, et. al.; GUANGXUE XUEBAO, Vol 5 No 10, Oct 85).....	8
1.3J Output Obtained From XeCl Excimer Laser (Cheng Xusan, et. al.; GUANGXUE XUEBAO, Vol 5 No 10, Oct 85).....	14
Velocity Distribution of Atomic Beams Measured (Wang Yuzhu, et. al.; ZHONGGUO JIGUANG, Vol 12 No 11, 20 Nov 85).....	21
Nuclear Design for Qinshan 300 MWe PWR Power Plant (Tang Bowen, Zhang Yongqian; HE KEXUE YU GONGCHENG, Vol 5 No 2, Jun 85).....	26
Progress in Plasma Focus Research (Yang Jinji, Han Min; HE KEXUE YU GONGCHENG, Vol 5 No 2, Jun 85).....	39
'Screen' Editing Program in Chinese (Mei Miaoping; XIAOXING WEIXING JISUANJI XITONG, No 2, 8 Feb 85).....	52

ABSTRACTS

APPLIED SCIENCES

HE KEXUE YU GONGCHENG [CHINESE JOURNAL OF NUCLEAR SCIENCE AND
ENGINEERING] Vol 5 No 2, Jun 85.....

57

APPLIED SCIENCES

SPECTER OF WAR IN SPACE DISCUSSED-PART II

Beijing HANGTIAN [SPACEFLIGHT] in Chinese No 6, Nov 85 pp 8-11

[Article by Bao Xianmin [7637 7359 6900]. For related material see JPRS-CST-86-004 of 28 Jan 86]

[Text] (IV) Anti-Satellite Weapons

In the fall of 1968, the Soviet Union launched an artificial satellite "Cosmos 249" into an elliptic orbit from the Tyuratam base near the Aral Sea. But shortly afterwards, the satellite drifted away from its perigee at 500 km altitude and exploded. Ten days later, the "Cosmos 252," which was launched into a similar orbit, also disappeared after an explosion.

Prior to that time, the "Cosmos" 248" satellite had been launched into a 500-km circular orbit. It turned out that the explosions of "Cosmos 249" and "Cosmos 252" occurred after the satellites had approached and rendezvoused with "Cosmos 248." Later it was discovered that these were actually Soviet tests in which fragments from an exploding satellite were used to destroy enemy satellites.

Subsequently, the Soviet Union had tested other attack strategies: for example, attacking the target satellite from the same circular orbit; approaching the target satellite from an elliptic orbit before attacking; and attacking the target by a sudden climb maneuver without entering the target satellite orbit. In June 1982, the Soviet Union conducted a space war exercise which greatly surprised the United States. During the exercise, intercept satellites were first launched to destroy U.S. reconnaissance satellites and communications satellites; at the same time the satellites were being attacked, two ICBM's, an SLBM, an IRBM, the SS-20 and an anti-ballistic missile were also launched.

The Soviet exercise showed that war in space will be the preamble to a large-scale nuclear war on the ground. The U.S. Department of Defense pointed out that the Soviet exercise was "based on a first-strike offensive strategy," and believed that Soviet intercept satellites had already developed to the stage where they are ready to be deployed. In response to this threat, the United States also accelerated its research and development of anti-satellite weapons.

On 21 January 1984, an F-15 fighter aircraft carrying satellite intercept missiles took off from Edwards Air Force Base in California. The intercept missile was 1.5 m long and 0.3 m in diameter. When the aircraft reached the missile test site near the Vandenberg Air Force Base, the missile was launched into space. This was the first test of an air-launched anti-satellite weapon powered by a two-stage rocket: the first stage was a close-range missile built by the Boeing Co.; the second stage was a rocket built by the (?Vaught) Co. The warhead contained 56 small rockets and the range was approximately 1,400 km.

Although the details and results of the test were not released, it is possible to get an approximate idea from information published in the open literature. First, the F-15 climbs to an altitude of 25 km and launches the missile. Controlled by an inertial guidance system equipped with laser gyroscopes, the missile travels toward the target along a predesignated flight path. The missile is equipped with long-wavelength infrared sensors for detecting enemy satellites and 8 aiming telescopes; once an enemy satellite is detected, it automatically begins tracking the target and then destroys it. The rocket carrying the warhead has a propulsion system which can control the attitude to ensure hitting the target. The warhead itself also spins at a speed of 20 revolutions per second to maintain attitude stability. The main advantage of this type of missile is that it can [come] closer to the orbit of the target satellite than an anti-satellite weapon launched from a ground site, and it has a very high degree of mobility. While it can only attack low-orbit satellites, it has a better chance of being implemented earlier than particle beam weapons or laser weapons. The United States has decided to begin initial deployment of such anti-satellite weapon before 1987, and complete the final deployment by 1989.

(V) Military Application of Space Shuttle

On 12 April 1981, the space shuttle began its first flight from the Kennedy Space Center in Florida. Twenty minutes after lift-off, the Soviet press agency TASS issued a report about the launch with the following remarks: "Hiding under the cover of scientific research, the space shuttle is actually part of the plan of the U.S. Department of Defense to extend the arms race to a region above the atmosphere"; "Its main objective is to perform laser weapon tests and to establish a base for launching spy satellites."

There was a good reason why the Soviet Union was so sensitive about the space shuttle.

Initially the United States had a plan to build a powered glider which can carry one person and be launched into orbit by a large rocket. After orbiting the earth several times, it can re-enter the atmosphere and glide back to the base using its delta wing. This plan was abandoned in 1963, but subsequent designs of the space shuttle were remarkably similar to this original plan.

The space shuttle is approximately 37 m long, 24 m wide and 14 m high; it can carry as many as seven passengers. It is capable of sending a 29-ton object into a 28° inclined low-earth orbit. It was designed in 1971 according to a basic plan established jointly by NASA and the Department of Defense. The most critical part of the space shuttle is the variable delta wing, which not only has good high-speed performance in space but also allows the space shuttle to glide back to the base after re-entering the atmosphere.

In trying to destroy the target satellite, a Soviet intercept satellite must first determine its orbit; in other words, the intercept satellite must follow the target for several orbits before approaching it. Therefore, if the space shuttle can circle the earth just once in a polar orbit to perform its reconnaissance mission, and re-enter the atmosphere to land at a convenient location, then the manned reconnaissance satellite can avoid being attacked. This is one of the U.S. Department of Defense's objectives in designing the space shuttle.

The United States conducted an ultra-low temperature infrared sensor experiment on the space shuttle launched in June 1982. Although the experiment failed because the sensor cover was not removed, it nevertheless was the first test of a space weapon system. Many experiments on the space shuttle are for military purposes; in the flight plans which have been announced today, 35 percent of them are military experiments.

In April 1984, the space shuttle Challenger successfully captured and repaired a solar observation satellite. The success of this mission would not have been possible without the aid of military imaging satellites. However, in order to launch a large number of military resources into space for the purpose of destroying enemy satellites and eliminating interferences, the space shuttle is absolutely essential. In March 1980, during a testimony by the Secretary of the Air Force to the Armed Services Committee of the U.S. Congress, he said: "We expect the space shuttle to play a revolutionary role in military applications." In September 1982, the Department of Defense established an Aerospace Command for managing the use of space shuttles; it will become the center for monitoring space activities and defending against attacks by hostile countries.

(VI) Space Bases

In the early 1960's, the United States built three huge radar bases in Alaska, Greenland and England to form an early-warning network to monitor ICBM's attacking North America. These radars lie on a circular arc which extends across the North Pole and surrounds the Soviet landmass.

Both the United States and the Soviet Union had deployed a tracking network near the North Pole to allow their own ICBM's to attack the opponent by traveling along the shortest distance over the Arctic Circle. In November 1967, U.S. Secretary of Defense MacNamara revealed a new Soviet plan to develop nuclear weapons which attack over the South Pole, and he gave the following description of the Soviet test:

First, an artificial satellite carrying nuclear warheads is launched into a 160-km low-earth orbit; then, before completing one circle around the earth, it fires rockets in the opposite direction to attack targets on the ground. To travel the same distance, it takes much less time for the satellite to reach the target than for an ICBM which flies along a parabolic trajectory with an apogee of 1,000 km. Therefore, by disguising itself as a satellite, this weapon can mount a surprise attack over the weakly defended South Pole region.

This new weapon was called the Fractional Orbit Bombardment System (FOBS). But, before it reached the deployment stage, the FOBS was terminated because it must travel through the atmosphere for a long period, which degrades its targeting accuracy due to air resistance. Furthermore, the reinforcement of air defense network has greatly reduced the effectiveness of the surprise attack. However, the Soviet Union had other intentions behind the FOBS experiment.

About a month before MacNamara announced the Soviet FOBS plan, he proposed the ratification of the "Space Treaty" which limits the use of space, the moon, and other celestial bodies for peaceful purposes. Article 4 of the treaty, which is related specifically to military activities, "prohibits objects which carry nuclear weapons or other weapons with massive destructive power from being sent into an earth orbit." The key phrase "earth orbit" is designed to exclude ICBM's from the treaty. On the other hand, objects that do not complete one earth orbit or satellites that are only in a partial orbit are not considered violations of the treaty even if they carry weapons with massive destructive power. Therefore, it is natural to consider using FOBS as the initial "attacking satellites" in a space war.

The treaty also has other loopholes. The so-called "weapons of mass destruction" refer to only nuclear weapons, chemical weapons and biological weapons; other weapons are exempt from the treaty. Also, while the treaty specifically "prohibits the establishment of military bases, military facilities or defensive facilities or any form of weapon tests or military exercises in space," it does not rule out military bases in orbit.

The space shuttle has taken full advantage of these loopholes. President Reagan also talked about bases and stations in space in his 1984 new year's speech. The plan was to establish a base carrying 6-8 personnel and an unmanned platform which can monitor the entire earth surface from a 400-km earth orbit. The space shuttle will be used to provide transportation between the earth and the space station.

In 1981, in articles discussing the rendezvous between the Soyuz 6 space station and the artificial satellite Cosmo 1267, several U.S. aerospace magazines pointed out that "the satellite had a device capable of ejecting small flying objects," and "its mission was actually to eject and retrieve small objects."

It was unclear whether or not this was an anti-satellite satellite (ASAT), but one thing was certain: both the United States and the Soviet Union were trying to make maximum use of space for military purposes. Reportedly, in 1982 the Soviet Union also began scale model tests of a space shuttle; a cuttlefish-like, unmanned satellite with wings was seen to have landed in the Indian Ocean. In December 1983, the Soviet Union conducted another scale model test of the space shuttle.

(VII) Electronic Reconnaissance Satellite

On 17 April 1984, an incident occurred in London where a member of the Libyan liaison office used a machine gun to shoot at people in a parade. According to a report by the ABC television network in the United States, before the incident took place, the Libyan Government had issued a directive to the Libyan liaison office in London which said: "We cannot sit still and watch a parade protesting against Qadhafi." The United States knew about the directive and immediately notified the British Government. But the tragic incident took place before the situation was clarified; one female police officer was killed and many people in the parade were injured.

The "directive" was intercepted by a U.S. electronic reconnaissance satellite which was monitoring the telephone conversation between the Libyan Government in Tripoli and the liaison office in London. This incident reveals the role played by reconnaissance satellites in intelligence warfare.

Most electronic reconnaissance satellites are in 300-500 km, near-circular orbits; their mission is to determine the location, wavelength and performance of enemy air defense radars, and to collect electronic intelligence such as radio communications between military bases, troops and warships. The intelligence about the anti-Qadhafi parade in London was only a very small part of the mission.

In September 1983, at the time when Soviet fighters shot down a South Korean passenger plane, an electronic reconnaissance satellite also became the center of attention. The Soviet Union claimed that when the Korean airplane invaded Soviet air space, it was "carrying out spy activities" by coordinating with a U.S. electronic satellite located above the Kamchatka-Sakhalin area.

Although the truth remains unknown, one thing is clear: in order to take control in electronic warfare, it is essential to determine the wavelength and decipher the code used for radio communications in a crisis situation. Whether or not the Soviet accusation was accurate, this incident demonstrates the importance of electronic reconnaissance satellites.

(VIII) Photographic Reconnaissance Satellites

On 16 October 1964, three major world events took place: Khruschev was removed from office; the British Labor Party won in the general election; and the first atomic bomb was successfully exploded in China.

The Chinese nuclear test had been predicted 20 days before it actually happened. On 29 September, the U.S. Secretary of State Rusk issued a special message stating that "China will conduct a test of its first nuclear explosion in the near future"; it also said that if the test was to take place, "the United States will be able to detect it."

The U.S. Government did not reveal the source of this intelligence; it was referred to only as "various intelligence network." In fact, this was another important achievement of the newly deployed U.S. photographic reconnaissance satellite.

In the past, aerial reconnaissance had been carried out primarily by airplanes. The Cuban crisis in October 1962 created extreme tension between the United States and the Soviet Union. The crisis began when the so-called "Black Spy Plane" U-2 detected Soviet IRBM's being shipped to Cuba.

The development of surface-to-air missiles made it very difficult to continue using aircraft to carry out aerial reconnaissance. In May 1960, a U-2 surveillance plane was shot down by surface-to-air missiles over the Soviet Union; as a result, the scheduled summit conference between the U.S. and Soviet heads of state was cancelled. Since this incident, an increasing amount of attention was given to the idea of conducting surveillance missions in space in order to avoid the threat of surface-to-air missiles.

The United States had initiated the research and development of a photographic reconnaissance satellite at a very early date. In 1955, the U.S. Air Force proposed the basic concept of such a satellite, and asked several companies to perform technical feasibility studies of implementing this idea. Actual deployment of the satellite began with the "Discoverer" in 1959. Because of the limited launch capabilities at that time, only two types of satellites were deployed: one was a general surveillance designed to perform broad-area search and surveillance; the other was a detailed surveillance satellite capable of taking high-resolution photographs of specific targets. In 1971, a reconnaissance satellite called the "Big Bird" was launched by the Atlas 3D rocket which had the capability of sending a 13-ton object into low-earth orbit; this satellite could perform both general surveillance and detailed surveillance functions and was referred to as Project 467. Reportedly the satellite had six retrievable sealed film containers; the exposed films could be retrieved from air drops or the content could be sent back to the ground via electric transmission. The satellite was equipped with small rockets which were used to lower the orbit for carrying out detailed surveillance. Initially, the Big Bird had a design life of 50 days; 5 years later it was extended to 1 year. The KH-11 model of the satellite had a design life of over 2 years.

The development of photographic reconnaissance satellite in the Soviet started a few years later. The first satellite was launched in 1962. It is difficult to determine the status of Soviet military satellites because they are launched as part of the "Cosmos" series. However, based on the inclination and altitude of the satellite orbit, and from analysis of the signals transmitted by the satellite, one can get a general idea of their characteristics. Like the U.S. versions, the Soviet Union initially also had two different models: one for general surveillance and the other for detailed surveillance; later,

satellites with their own propulsion systems were developed. The main difference was that the Soviet satellites had a maximum life of approximately 40 days; as a consequence, the Soviet Union had to launch a large number of satellites into space.

Whenever a major international incident took place, for example the India-Pakistan war in 1971, the 4th Mideast War in October 1983, the Soviet invasion of Afghanistan in December 1979, and the Falkland Islands conflict in the spring of 1982, reconnaissance satellites would appear over the region of interest to perform their mission.

(IX) Mapping and Navigation Satellites

The next-generation ICBM being developed by the United States, the MX, has a range of 1,000 km; one out of two missiles can hit its target with an accuracy of 120 m. The Tomahawk cruise missile has a range of 3,200 km and a miss distance of 30 m. To achieve such remarkable accuracy requires the use of mapping satellites to construct high-precision maps.

It is well known that the earth is an oblate spheroid with a slight flattening near the North and South Poles. This results in irregular distribution of gravitational forces which affect the targeting accuracy of ICBM's. Because if the gravitational forces from the left and right sides of the flight path are not equal, the missile will be pulled by the stronger gravitational force and deviate from its course. Therefore, it is necessary to accurately measure the gravitational distribution around the globe, which also must rely on mapping satellites.

The NAVSTAR Global Positioning System being developed by the United States consists of an 18-satellite constellation. With a navigation accuracy of 16 m, it will play an important role in determining the positions of nuclear submarines and strategic bombers, and in correcting navigation errors along their course of travel.

Ocean surveillance satellites have the task of monitoring warships. In order to perform its mission in both daylight and darkness, and under all weather conditions, the satellite is equipped with radars which can collect electronic intelligence such as transmissions from shipborne radars and radio communications. One of the outstanding features of the ocean surveillance satellite is its ability to detect nuclear submarines using infrared sensors. No matter how deep the submarine is submerged below the ocean surface, the warm water ejected by the atomic reactor and the ripples generated by the propellers will eventually propagate to the ocean surface. Therefore, by surveying the ocean using infrared sensors capable of measuring minute temperature differences, it is possible to follow the track of a submarine. But this is only a theoretical concept, the actual capability of such sensors remains a top military secret.

The space war concept being pursued by both the United States and the Soviet Union will turn a new page in the history of space exploration. Indeed, space exploration goes hand-in-hand with military expansion.

LIFETIME OF EXCIMER LASER STUDIED

Shanghai GUANGXUE XUEBAO [ACTA OPTICA SINICA] in Chinese Vol 5 No 10, Oct 85
pp 881-885

[Article by Hu Xuejin [5170 7185 6855], Zhao Zhensheng [6392 7201 5116],
Li Zhaolin [2621 2507 5259], and Che Mingyu [6508 2494 3842]: "Study on the
Operating Lifetime of an Excimer Laser"]

[Text] Abstract: Long-term stable operations of XeCl excimer lasers depend considerably on the depletion of HCl. Our experiments have shown that the lifetime of such device can be extended significantly by adding appropriate amount of an inexpensive donor gas HCl into the laser chamber made of epoxy resin pipe. In this way, more than 1.03×10^6 pulses were obtained by one filling of Xe and Ar and then replenishing HCl at several appropriate times. For a repetition rate of 5.3 pulses per second and single-pulse energy of 100 mJ, the laser was still able to operate normally after working continuously for 54 hours. The maximum single-pulse energy of the laser was 160 mJ. The influence of the content of HCl on the output characteristics of the laser was also studied.

I. Introduction

Improvement of the performance and lifetime of XeCl excimer lasers is a general concern. There are many factors affecting the lifetime of an excimer laser, including changes of the laser medium, contamination of the gas, erosion of the laser material and damage of the optical components.¹ Under normal circumstances, the depletion of the HCl gas and the contamination of the working gas by the chemical reaction products play an important role in shorting the life of the laser, especially in the presence of water vapor impurities. The lifetime of the laser may be extended if the moisture content and the purity of HCl are rigorously controlled and a suitable amount of HCl is replenished when the laser output energy is degraded to a certain level. Using laboratory prepared HCl gas, we obtained more than 100 mJ of output and a maximum energy per pulse of 160 mJ from a water-cooled cylindrical excimer laser. After one filling of Xe gas and buffer Ar gas, we obtained more than 1×10^6 pulses at a repetition rate of 5.3 pulses per second.

II. Experimental Setup

The working principle of the excimer laser is illustrated in Figure 1. The laser tube is an epoxy tube with an outer diameter of 18 cm and a wall thickness of 1 cm. The main electrodes are a pair of nickel plated brass electrodes with $R = 20$ mm, an effective discharge length of 830 mm and an electrode gap of 20 mm. The storage capacitor C_s consists of 26 2700 pF induction free capacitors in parallel. The ultraviolet preionization sources are located on the two sides of the main electrodes in the form of two rows of 24 pairs of spark pins parallel to the main electrodes. Each pair of spark pins are connected to a 780 pF capacitor. The resonance cavity consists of an aluminum plated total reflection mirror with a radius of 3 m and a flat quartz output mirror, the circulation between the gas storage tank and the laser tube is of the longitudinal type. Several meters of copper tubing for the cooling water are situated inside the gas storage tank. The entire system is shown in Figure 2.

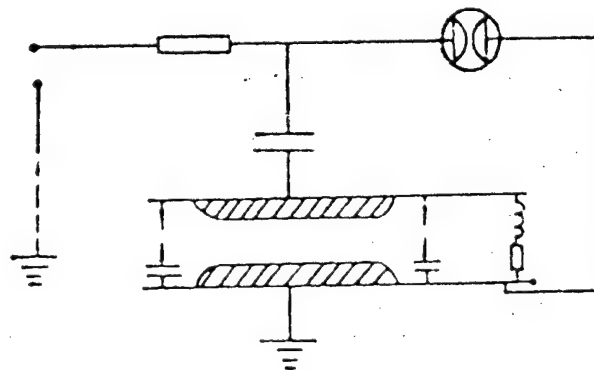


Figure 1. Schematic Diagram of the Laser

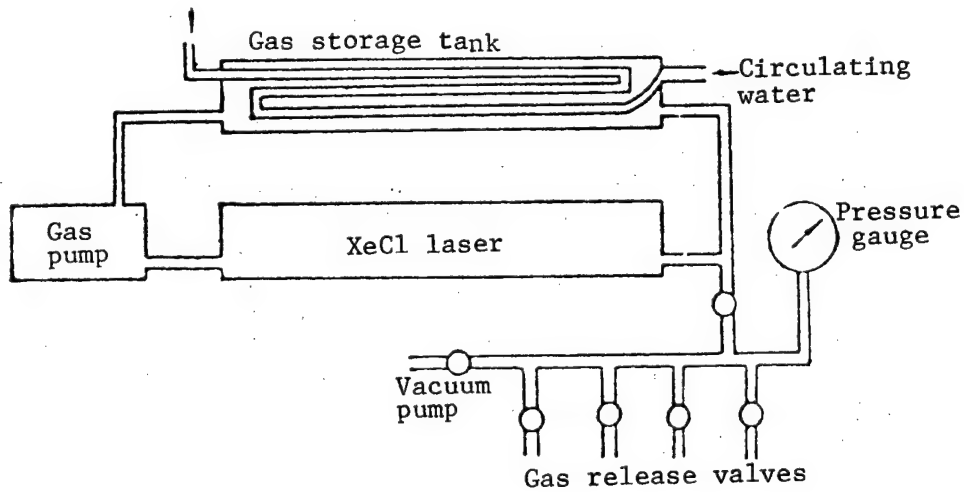


Figure 2. Setup of the Laser System

III. Results and Discussion

A number of factors affect the lifetime of a XeCl excimer laser. We follow the following two approaches to improve the life of excimer lasers: (1) optimize the mixture ratio of the laser medium based on the dynamics of the excimer laser and the test results; (2) augment the gas mixture optimization with auxiliary steps such as improving the circulation system, the gas storage reservoir, and the water cooling system.

Figure 3 shows the output laser energy E as a function of lifetime τ for two different gases in an excimer laser equipped with a circulation system but without a gas storage reservoir. For a mixture ratio of $\text{Xe:HCl:Ar} = 36 \text{ Torr:} 1.35 \text{ Torr:} 1.35 \text{ atm}$, the initial output energy E is about 42 mJ. After the first filling and 1×10^5 pulses, the energy drops to about one-half of the initial value.

(A) ● No circulation, $P = 1.4 \text{ atm}$, $V = 32 \text{ kV}$
 (B) ▲ With circulation, $P = 1.35 \text{ atm}$,
 $V = 28 \text{ kV}$
 + Adding gas

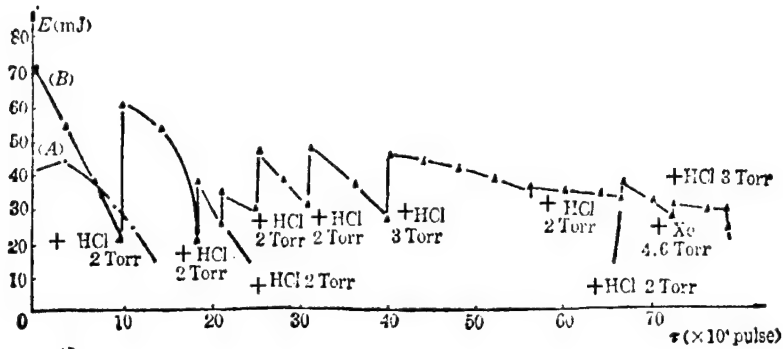


Figure 3. Lifetime Curve of XeCl Excimer Laser With No Gas Reservoir

Figure 4 shows the output laser energy E as a function of the lifetime τ for two gas mixtures in a XeCl excimer laser equipped with a gas reservoir (but without water cooling). For a mixture ratio of $\text{Xe:HCl:Ar} = 40 \text{ Torr:} 8 \text{ Torr:} 1.3 \text{ atm}$, the initial output energy E is about 140 mJ. After the first filling and 3.8×10^5 pulses, the energy drops to about one-half the original value. After three replenishments of HCl, the output energy is restored to 100 mJ each time and an additional 1.5×10^5 , 2.8×10^5 , and 2.1×10^5 pulses are obtained after the respective replenishments. After delivering a total of 1.03×10^6 pulses, the output energy is still 70 mJ or so. At a repetition rate of 5.3 pps, the device operated continuously for 54 hours. The life curve (E versus τ) is shown as curve (A) in Figure 4. Using the gas mixture ratio above, and using a voltage of 37 kV, the output energy E is about 160 mJ.

(B) ● No water cooling, $P = 1.3$ atm, $V = 30$ kV
 (A) ▲ With water cooling, $P = 1.3$ atm,
 $V = 30$ kV
 + Adding gas

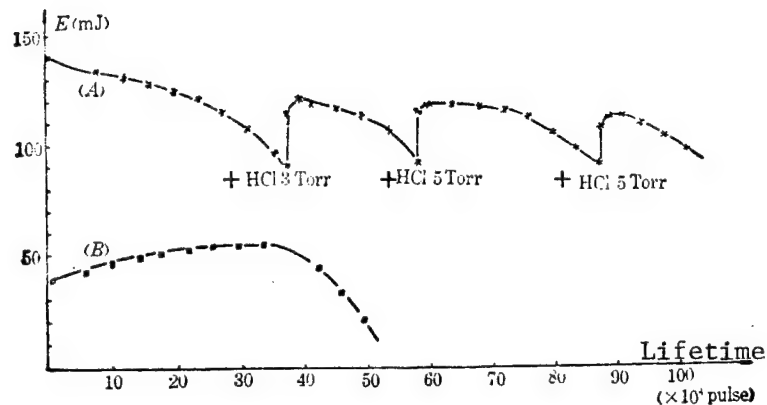


Figure 4. Lifetime Curve of XeCl Excimer Laser With Gas Reservoir

The curves in Figure 4 are experimental results obtained using a XeCl laser with a gas mixture ratio of Xe:HCl:Ar = 35 Torr: 15 Torr: 1.3 atm and equipped with a water cooling gas reservoir. The curves clearly show that the output energy decreases as the HCl content increases. The lifetime for one gas filling is about 4.5×10^5 pulses.

Both the theory and the test results show that there is an optimal mixing range for the inert gas Xe and the halogen donor HCl in the generation of the XeCl laser. The HCl donor has an optimal concentration for the formation of the XeCl excimer. Excessive or inadequate HCl lead to a lower output energy.² The reaction formula³



shows that when the HCl concentration is too high, the excitation of XeCl^* increases. On the other hand, since HCl has a greater electron affinity, it may cause instability of the discharge. In the reaction



the adsorption of electrons depends on the HCl concentration. At a higher HCl concentration, the electron density is lower and the discharge resistance is higher. A decreasing electron density leads to discharge instability, higher resistance, and less energy injected into the laser medium.³ Both effects decrease the output laser energy and serve to explain the experimental results shown as curve (A) and curve (B) in Figures 3 and 4. When the HCl content is low, there is not enough Cl donors and, as a result, the number of XeCl^* molecules decreases and the output energy is low. This is consistent with the results of curve (B) in Figure 3.

In the early operating period of the laser, the lifetime degradation is caused by the depletion of the HCl gas. In this period the gas contamination problem is not as serious as the laser material erosion problem. In the ultraviolet preionization zone and the discharge zone, the HCl reacts with the metal parts under the discharge conditions and produces metal chlorides such as CCl_4 , FeCl_3 , SiCl_4 , PCl_3 , and AlCl_3 . Hydrocarbon chlorides form on the insulating materials used in the laser such as epoxy, organic glass, and o-ring seals. The formation of the chlorides causes deposits to form on the optical surfaces and also corrodes the materials. After a period of operation, white deposits are found on the cavity plates and black sticky deposits are found on the surface of metal parts, especially below the UV light source. Such reactions seriously deplete the HCl gas and contaminate the device. In the early phase of the operation after the first filling of the gas, the contamination of the gas medium is not serious. Curve (A) in Figure 4 shows that the output energy drops to one-half of its initial value after 3.8×10^5 pulses. When 3 Torr of HCl is replenished at this point, the output energy is restored to about 75 percent of the original level. This result lends support to the analysis above. However, after repeated HCl replenishments and a long period of operation, the gas contamination accumulates to such a level that the lasing action may be quenched. As shown in Figure 3(B), the output energy can no longer be increased after 10 replenishments of 3 Torr of HCl and the laser output vanishes soon after.

After the laser has delivered 10^6 pulses, rectangular spots of the same size as the laser spot can clearly be seen on the quartz window and on the aluminum platted total reflection mirrors. They are actually particle damages due to the chemical corrosion and the laser action. After replacing all the gas medium, the XeCl laser is again obtained but the output is lower than before. The window damage and the mirror damage are therefore not the fundamental causes that end the service life of a laser. What eventually quenches the lasing is the contamination of the working medium in the laser tube.

By comparing the results in Figures 3 and 4, one finds that the lifetime of a laser equipped with a gas reservoir is longer than that without a gas reservoir. Curve (A) in Figure 4 shows that water cooling and high purity HCl gas are beneficial to the extension of the service life of the laser and to the ability of maintaining a stable output.

The results of curves (A) and (B) in Figure 4 show that, for one filling of the gas, a higher HCl pressure will provide a lower and more stable output energy for a longer time. Based on the analysis above, the output energy is not high when the HCl content exceeds the optimal mixture ratio. After delivering a large number of pulses, the HCl content gradually approaches the optimum ratio but at the same time the gas contamination is also becoming more serious. The former increases the laser output energy and the latter decreases the output energy. In the early phase of the operation, the gas contamination is still not very serious and the net result is therefore an increase of the output energy. As the laser delivers more and more pulses, the HCl content will become less than that of the optimal ratio, and the contamination of the working gas continues to accumulate. The combined effect is that the laser

output energy passes through a maximum and begins to decline, as shown in Figure 4(B).

IV. Conclusions

To improve the service life of a XeCl laser, one should keep the moisture content of the device low, use high purity HCl gas, and equip the laser with a water-cooled gas reservoir. These measures can effectively decrease the corrosion of the metal parts and the contamination of the gas medium. When the HCl is depleted to a certain level, the gas should be suitably replenished to restore the optimum ratio and the output energy. The service life of the laser may be extended by using some inexpensive HCl gas without replenishing the expensive Xe gas. These methods are practical and economical.

The results and experience gained in these experimental testing will prove valuable in extending the service life of excimer lasers and raising the output energy.

The authors thank Ku Geng [1655 5087], Huang Ximming [7806 2946 2494], Yang Liu [2799 2692], Li Daqiao [2621 1129 2890], and Zhang Wanqing [1728 8001 3237] for their participation in this work.

REFERENCES

1. LASER FOCUS, 17(10), 65, 1981.
2. Private communication.
3. Hirokazu Hokazono, et al., J. APPL. PHYS., 56(3), 680, 1984.

9698/9365

CSO: 4008/24

1.3J OUTPUT OBTAINED FROM XeCl EXCIMER LASER

Shanghai GUANGXUE XUEBAO [ACTA OPTICA SINICA] in Chinese Vol 5 No 10, Oct 85
pp 865-869

[Article by Cheng Xusan [2052 1645 0005], Lou Qihong [2869 4388 3163], and Wang Runwen [3769 3387 2429]: "Injection Locking of a XeCl Excimer Laser With Pulse Output Energy of 1.3J"]

[Text] Abstract: The injecting locking of a XeCl excimer laser driven by a long transmission-line pulse-forming network was achieved with an unstable optical resonator. The injection-locked output energy was 1.36J (18 MW in peak power) with a linewidth of 8.9×10^{-8} Å and a beam divergence of 0.2 m rad. Parameters of the injection locking and synchronization characteristics of discharge are also discussed.

I. Introduction

The bandwidth of an excimer is usually 10 Å or more and it is therefore difficult to obtain high power narrow spectral line output from a single unit. Applications in laser chemistry, isotope separation, and nonlinear optics,^{1,2} on the other hand, not only call for high power but also narrow spectral line ($\leq 10^{-2}$ Å). The most effective method for producing a high power narrow line output available today is injection locking. In this method a beam of low power and narrow linewidth laser with good spatial coherence is injected into a high power oscillator to control its spectrum and spatial divergence angle.

The injection locking of excimer lasers has been reported in the literature.³⁻⁵ In this work, we have for the first time used X-ray preionization, water transmission line charging, and multichannel switching to control the main discharge pump oscillator and achieved the injection locking of a XeCl laser using a novel discharge synchronization circuit. Our goal is to further improve the output power and linewidth. We have also compared the output beam characteristics for different optical cavity structures.

II. Experimental Apparatus for Injection Locking

Figure 1 shows the laser injection locking apparatus. The injection source is an ultraviolet preionization XeCl laser, F_1 , F_2 , and F_3 are etalons, D_1 and D_2 are diffraction gratings, M_{10} and M_{20} are coupling cavity mirrors. The oscillator is an X-ray preionization unit, M_1 and M_2 form a confocal unstable cavity, F is a thin quartz plate that seals the 5 mm diameter orifice at the center of the cavity plate M_1 , and D is the injection hole. The details of the injection source and the oscillator installation are given in References 6 and 7.

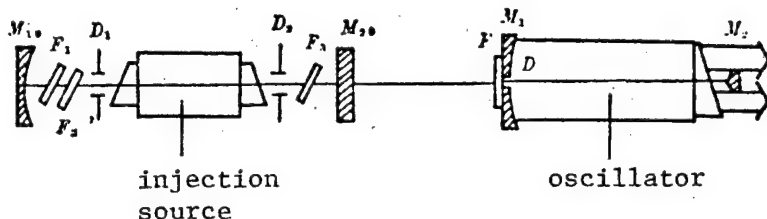


Figure 1. Schematic of the Optical Setup Used for Injection Locking

1. Injection source

In order to suppress the linewidth, three etalons (F_1 , F_2 , and F_3) are inserted into the injection source cavity. F_1 and F_2 are, respectively 0.1 mm and 0.2 mm thick and have a reflectivity of 75 percent. F_3 is 1 mm thick and has a reflectivity of 90 percent. A 3 mm diameter pinhole collimator is used to obtain an output with a linewidth of $8.9 \times 10^{-3} \text{ \AA}$, a spatial diffraction angle of 0.15 m rad, a full width at half maximum of 25 ns, a maximum single pulse energy of 200 μJ and a peak power of 8 kw.

As an excimer laser injection source, the output power only needs to be slightly higher than the single mode spontaneous emission power of the oscillator for injection locking.⁸ The X-ray preionization oscillator used in our experiment has a XeCl linewidth $\Delta\lambda=10 \text{ \AA}$, an amplification medium length of $L = 60 \text{ cm}$, and an effective aperture $D^2=10 \text{ cm}^2$. The theoretically calculated equivalent spontaneous radiation noise signal⁸ is about 10 W/cm^2 . The 8 kw injection signal power is therefore adequate for injection locking.

2. Oscillator

The oscillator is a semi-external normal branch confocal unstable cavity. The purpose of using an unstable cavity is to improve the directivity of the beam and lower the threshold power of injection locking.⁸

The injection end is a total reflection concave mirror with a radius of curvature of $R_1 = 300 \text{ cm}$. The effective reflection aperture is $a_1 = 4 \text{ cm}$, and the cavity mirror is the window of the discharge chamber. The output end has a ring coupler. The quartz plate of the discharge chamber window is coated on both sides with antireflecting coating to produce a total reflectivity less

than 2 percent. The window is tilted from the axis by more than 3° . The output coupling mirror is a total reflecting convex mirror with an effective radius of $a_2 = 0.8$ cm and a radius of curvature of $R_2 = -90$ cm. The length of the confocal cavity satisfies the following relationship: $L = 105$ cm $\pm \Delta L \approx f_1 + f_2$, $f_1 = R_1/2$, and $f_2 = R_2/2$. The cavity length increment $\Delta L \approx 0.5$ cm adjusts the equivalent Frisnel number N_{eq} of the cavity and the cavity loss so that the injected beam is matched to the unstable cavity and the injection threshold power is a minimum. The equivalent Frisnel number of the cavity is

$$N_{eq} = \frac{c_2^2}{4\pi L} \left[\frac{R_2}{a_2} (\beta_2 g_2 - 1) \right]^{1/2} \approx 50.$$

where $g_1 = 1 - \frac{R_1}{2} = \frac{2}{3}$, $g_2 = 1 - \frac{R_2}{2} = 2.2$. The magnification of the unstable cavity is $M_{un} = \frac{R_2}{R_1} = 3$.

As shown in Figure 1, the injection beam is introduced through a small circular hole drilled at the center of the convex mirror. A 1 mm thick quartz plate is glued behind the mirror, and the diameter d of the small hole is 5 mm. Since d is greater than the cross section of the injection beam (0.25 to 0.3 cm), the injection beam loss is only about 10 percent attributable to the reflection loss of the quartz plate. Also, because the divergence angle of the injection beam is approximately equal to the diffraction limit, the spatial divergence angle of the output beam from the main oscillator may be nicely controlled. The energy loss of the oscillator output due to the small injection hole is less than 10 percent of the total laser energy.

3. Synchronization of the main discharges

Since the width (FWHM) of the injection beam is 25 ns and the risetime of the leading edge of the oscillator is 10-20 ns and the pulse width is 70 ns, the time delay $\Delta\tau_j$ between the injection light and the oscillator gain must be less than 20 ns for injection locking to be possible. In other words, the main discharge time delay of the two units must remain within 20 ns. In order to achieve injection locking at a high laser energy, we have made the following improvements to the electrical circuit.

(1) In excimer laser injection locking, the injection source and the oscillator are often equipped with symmetric fast discharge circuits to facilitate the synchronization of the main discharge of the two units. However, it is usually difficult to raise the output laser energy above 1J or so using such fast discharge circuits. In this work we raised the laser output beyond the 1J level by using water transmission line charging and pulse shaping. Since the water transmission line is charged with a triangular pulse and the charging time is as long as 1 μ s, trigger circuits or delay line cannot adequately control the spread of the discharge delay of the two units. By solving the synchronization problem, we were able to achieve a single pulse output energy of 1.36J in the injection locking of a XeCl laser. To our knowledge, this is the highest single pulse energy output from an injection locked XeCl laser to date.

(2) In order to reduce jittering, we used a low inductance triple gap field anomaly type of ball gap for the injection source main discharge. The trigger signal has a leading edge rise time smaller than 5 ns, a voltage greater than 30 kV, and a breakdown time jittering smaller than 2 ns. By controlling the gas pressure of the oscillator switch and the gap distance, the breakdown jitter time can be kept below 15 ns.

(3) A 60 kV peak voltage, 1 μ s pulse width triangular voltage is taken from the circuit before the main discharge switch of the oscillator. This signal is time delayed by an RC circuit and then fed through a ball gap with a low inductance, small gap distance and high nitrogen gas pressure for pulse shaping. The triangular pulse with a 1 μ s leading edge is transformed into a steep trigger signal with a 5 ns leading edge and a 30 kV peak voltage. This trigger signal is used on the triple electrode ball gap of the injection source main discharge. The injection source main discharge time delay may be adjusted by changing the loop resistance and capacitance of the RC circuit or the breakdown voltage of the pulse shaper circuit. By using such a self-coupled trigger circuit, the injection source-to-resonator discharge time delay may be controlled to within 20 ns and the delay time is continuously tunable within a range of 400 ns. Theoretical analysis and experimental results of this type of circuit are presented in Reference 9.

III. Results and Discussion

1. Spectral characteristics

When the injection source is used to suppress the linewidth and select single spectral lines, three quartz etalons 0.1 mm, 0.2 mm, and 1 mm thick are placed in the cavity to select the three vibrational transition lines 0-0 (3077.04 \AA), 0-1 (3079.61 \AA), and 0-2 (3082.10 \AA).⁷ Injection locking is achieved on two of the three spectral lines (0-1 and 0-2). The injection of the 0-0 line farthest away from the 0-1 and 0-2 lines is not so successful. The oscillator has a water transmission line in its main discharge structure. The pulse width is relatively wide (100 ns for a stable cavity). Spectral line injection away from the center of the gain curve pulls the gain center toward the 0-1 and 0-2 transition and broadens the line width because of the competition from the strong transition lines.

The linewidth of the injection light is 8.9×10^{-3} \AA and no relative broadening is observed. Figure 2 shows the interference ring of the injection locked output light. The linewidth is determined from the interference ring.⁷ Assuming the linewidth of the free oscillation is 16 \AA , then the narrowing ratio of the injection locked line is $16:8.9 \times 10^{-3} \approx 1.8 \times 10^3$.

2. Energy characteristics

When the total gas pressure in the oscillation discharge chamber is 4.8 atm and the storage capacitor⁹ is charged to a voltage of 40 kV, the maximum energy per single laser pulse from the X-ray preionization oscillator is 1.4J for a stable cavity. For an unstable cavity, the output is 1.12J without injection

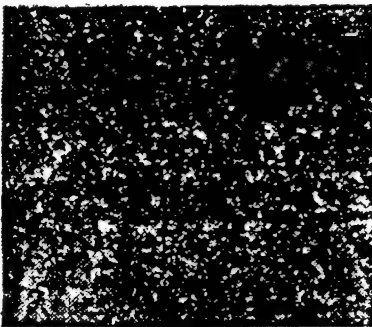


Figure 2. Interference Rings of Injection Locked Laser

locking and 1.36J with injection locking. The average output of the unstable cavity is improved by 25 percent with injection locking as compared to free oscillation. Figure 3 shows the unstable cavity laser output waveform with and without injection locking.

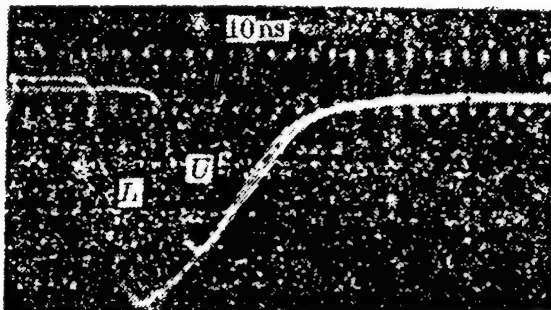


Figure 3. Laser Waveforms With and Without Injection Locking

L--injection-locked; U--unlocked XeCl (Time scale: 10 ns)

Without injection locking, it takes the oscillator at least 30 ns to establish the oscillation from the spontaneous radiation. With a strong (8 kw) injection signal, the oscillator may begin its oscillation directly from the injected signal and the oscillations may begin at least 20 ns sooner. The oscillator gain is fully used in the injection locking and the output energy is improved. The figure shows that the pulse width (FWHM) of the unstable cavity is 75 ns with injection locking and 50 ns without injection locking. The maximum output power with injection locking is 18 MW (1.36J, 75 ns).

Because the injection hole of the oscillator discharge chamber has a 1 mm quartz window, the gas pressure cannot be too high. The total pressure is generally 3.2 atm, the storage capacitor is charged to 35 kV and the injection locked output power is 11 MW (800 mJ, 70 ns).

The maximum narrow line output power of the injection source may reach 8 kw. By gradually decreasing the injection light intensity, the threshold power of the injection locked unstable cavity is measured to be 1 kw. When the

oscillator has a stable cavity ($R_1 = 3$ m, $R_2 = \infty$, and $L = 1.1$ m), injection locking was not achieved at an injection power of 8 kw. To achieve injection locking, the injection power is estimated to be the order of 80 kw or higher.

3. Spatial coherence of the light beam

The spatial coherence of the output laser of different cavity structures is compared using the 4×2.5 cm² cross-section output from an X-ray preionization discharged excimer laser.

Using a stable cavity ($R_1 = 3$ cm, $R_2 = \infty$, $L = 1.1$ m), the output energy is about 30 percent higher than that from an unstable cavity without injection locking but the spatial divergence angle is greater than 10 m rad. Using a subcritical F-P cavity ($R_1 = 20$ m, $R_2 = \infty$, $L = 1$ m), the divergence angle is reduced to 2 m rad and the output energy is about 5 to 10 percent higher than that from a stable cavity operated under the same conditions.

Using the unstable cavity shown in Figure 1, the divergence angle may be reduced down to 0.5 m rad but the output energy is also reduced. Using an unstable cavity for injection locking, the output energy is comparable to that using a stable cavity and the divergence angle can be reduced to 0.4 m rad or less. The focal spot on the photographic plate is no more uniform than that of unstable cavity injection locking.

To accurately measure the divergence angle of the unstable cavity output laser, the usual focal spot method is used. A series of circular apertures of different diameter are placed at the focal plane of an $f = 2$ m lens. The focused laser beam is allowed to pass the circular holes and the energy is measured behind the holes. Using an unstable cavity, about 80 percent of the laser energy enters a circular hole of 1.2 mm diameter with injection locking. Without injection locking, only 65 percent of the energy goes through. When the hole diameter is reduced down to 0.8 mm, 48 percent of the injection locked laser passes through the hole but only about 30 percent of the unlocked laser goes through the hole. This indicates that about one-half of the laser energy is concentrated in an aperture of 0.2 m rad (half angle).

Table 1. Laser Output Characteristics of Various Cavity Configurations

	Cavity length (cm)	Radius of curvature (cm)		Effective aperture of cavity mirror (cm)		Maximum output power	Maximum energy per pulse	Laser pulse width	Divergence angle (half width)
		R_1	R_2	a_1	a_2				
Stable cavity	105	300	∞	4	4	16.5MW	1.4J	85 ns	10 m rad
Critical cavity	100	2000	∞	4	4	16.5MW	1.4J	85 ns	1 m rad
Unstable cavity	105	300	-90	4	0.8	18MW	1.12J	60 ns	0.25 m rad
Unstable cavity injection locked	105	300	-90	4	0.8	18MW	1.36J	75 ns	0.2 m rad

REFERENCES

1. Armandillo, E., Proch, D., OPT. LETT., 1983, 8, No 10 (Oct), 523.
2. Leone, S.R., "Photofragment Dynamics," (in Advances in Chemical Physics, 50, K.P. Lawley, ed., 1982), 155.
3. Goldhar, J., Murray, J.R., OPT LETT., 1977, 1, No 6 (Dec), 199.
4. Goldhar, J., et al., IEEE, J.Q.E., 1980, QE-16, No 2 (Feb), 235.
5. Kannari, F., et al., APPL. PHYS. LETT., 1983, 42, No 9 (May), 777.
6. Lou Qihong, et al., private communication.
7. Cheng Xusan, et al., to be published in ZHONGGUO JIGUANG [CHINESE JOURNAL OF LASERS].
8. Bigio, I.J., et al., IEEE. J.Q.E., 1983, QE-19, No 9 (Sep), 1426.
9. Lou Qihong, et al., to be published.

9698/9365
CSO: 4008/24

APPLIED SCIENCES

VELOCITY DISTRIBUTION OF ATOMIC BEAMS MEASURED

Shanghai ZHONGGUO JIGUANG [CHINESE JOURNAL OF LASERS] in Chinese Vol 12 No 11, 20 Nov 85 pp 658-660

[Article by Wang Yuzhu [3769 5148 4554], Cheng Yudan [4453 5280 2481], Zhou Shanyu [0719 0810 6877], Huang Weigang [7806 4850 0474], and Liu Liang [0491 0081]: "Velocity Distribution Measurement of Atomic Beams by Means of Atomic Beam Deflection Under Resonance Light Pressure"]

[Text] Abstract: Measurement of the velocity distribution in an atomic beam by means of atomic beam deflection under resonance light pressure is reported. Both theoretical analysis and experimental results are given.

I. Introduction

The velocity distribution in an atomic beam is a fundamental parameter always encountered in the study of physics and chemistry using atomic beams. The velocity distribution is usually analyzed using a mechanical separator.¹ In recent years, spectroscopic methods have received increasing attention.²

Based on a multibeam atomic deflection technique,³ we have detected laser-induced atomic beam fluorescence using an optical multichannel analyzer and successfully measured the atomic deflection distribution. On this basis, we propose a method for measuring the velocity distribution using the atomic beam deflection under resonance light pressure.

II. Measurement Principle

As shown in Figure 1, both the incident beam and the beam reflected by mirror m_2 are perpendicular to the atomic beam. When the laser frequency is tuned to the resonance frequency, the beams exert a radiation pressure on the atoms. The beam reflected from mirror m_1 is not perpendicular to the atomic beam. Due to Doppler shift, it does not interact with the atoms. Under the resonant light pressure, the atomic beam undergoes a deflection in the z direction.

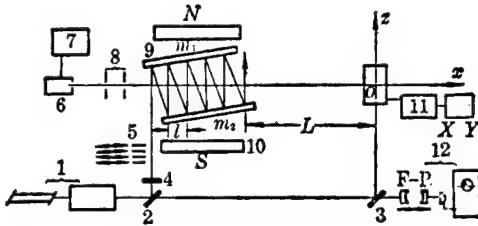


Figure 1. Schematic Diagram of the Experimental Setup

Key:

1. Tunable laser	7. Temperature control and monitor
2,3. Beam splitter	8. Collimator
4. $\lambda/4$ plate	9. Parallel plane mirrors
5. Attenuator	10. Magnetic field
6. Na furnace	11. OMA detection system
	12. Frequency monitor

The average total deflection in the z direction³ of an atom moving in the x direction with a velocity v , interacting with N_0 light beams and making a free flight over a distance L is given by

$$\langle z_{N_0} \rangle = \frac{\hbar K d N_0 f}{2 \tau m v^3} \left[\frac{l}{2} (N_0 - 1) + L \right] \quad (1)$$

where τ is the excited state life time of the atom, d is the light beam diameter, l is the distance between the light beams and the factor f for a two-level atomic system may be written as

$$f = ST_{(\Delta\nu)} / [1 + ST_{(\Delta\nu)}] \quad (2)$$

in which S is a saturation parameter and $T_{(\Delta\nu)}$ is a detune parameter. For an idealized collimated atomic beam in the x direction with a velocity distribution $j(v)$, the number of atoms with a velocity between v and $v + dv$ is $n(v) = j(v)dv$. Atoms with a velocity v will be deflected to $z(v)$. Let the distribution along the z axis be $g(z)$, we have

$$j(v)dv = g(z)dz \quad (3)$$

From Equation (1), we have

$$g(z) = \frac{1}{2B} \left(\frac{B}{z} \right)^{3/2} j(\sqrt{\frac{B}{z}}) \quad (4)$$

Under the interaction of N_0 light beams, we have

$$B = \frac{\hbar K d N_0 f}{2 \tau m} \left[\frac{l}{2} (N_0 - 1) + L \right] \quad (5)$$

In fact, the atomic beam has a certain cross-sectional profile in the absence of light interaction. If the original distribution of the atoms in the z direction is $F(z)$, then, under the action of N_0 light beams, the distribution becomes

$$G(z) = \int_{-\infty}^{\infty} \frac{1}{2B} \left(\frac{B}{t}\right)^{3/2} j(\sqrt{\frac{B}{t}}) F(z-t) dt \quad (6)$$

The relationship between the z direction distribution $G(z)$, the beam profile $F(z)$, and the velocity distribution $j(v)$ of the atomic beam deflected by the resonant light pressure is given by the convolution equation (6).

III. Measurement Results

The apparatus for measuring the atomic beam velocity using resonant light pressure deflection is already shown in Figure 1. The laser produces 16 light beams between a pair of parallel plane mirrors of high reflectivity. After passing through the collimator, the divergence angle of the N_a atomic beam is less than 2×10^{-3} rad. The deflection of the atomic beam takes place in a vacuum chamber under 4×10^{-6} Torr.

A ring dye laser pumped by an argon laser is operated in the single mode with a line width of 30 MHz. The frequency drift of the laser is monitored with an F-P scanning interferometer. The wavelength is 5890 Å. After passing through the $\lambda/4$ plate, circularly polarized light is formed. A magnetic field is applied at the interaction region. The sodium atoms are excited from the $3S_{1/2}(F=2)$ state to the $3P_{2/3}(F'=3)$ state to form a quasi-two-level system, thus avoiding the optical pumping effect.⁴

In order to subject the atoms moving at different velocity to the deflection effect of the resonant light pressure and to obtain laser-induced fluorescence, the interaction laser beams and the probing laser beam must all be perpendicular to the atomic beam. An He-Ne laser is used to simulate the atomic beam in aligning the optics. A grating is used to position the light beam and the orthogonality is accurately achieved, with an angle of deviation no greater than 10'.

The detectors are installed along the z axis and centered at point 0. When the laser is tuned to the resonance frequency of the sodium atom, 16 fluorescent light spots appear between the mirrors. The probing laser induced fluorescent light of the deflected atoms is imaged onto the detector of an optical multi-channel analyzer using a 1:2.15 camera lens system. The attenuator consists of four filter plates, their transmissivities for 5890 Å laser are respectively 90, 80, 67, and 40 percent. The filters are inserted into the optical path in different combinations so that light beams of different intensity are obtained. Figure 2 shows the distribution of the deflected atomic beam under four different experimental conditions. Curve 0 shows the original z direction distribution of the undeflected beam. Curve 4 shows the deflection distance is 7.74 mm and the deflection angle is 1×10^{-2} rad corresponding to the maximum of the deflected atomic distribution.

Using Equation (6) and curves 0 and 2, we have computed numerically the experimental and theoretical thermal atomic velocity distribution for the following experimental parameters: $d = 0.2$ cm, $l = 0.56$ cm, $L = 68$ cm, $N_0 = 16$, $T = 700$ K, and $I = 4$ mW. The results are shown in Figure 3. The number of slow atoms has clearly decreased. Consequently, if we make the assumption that

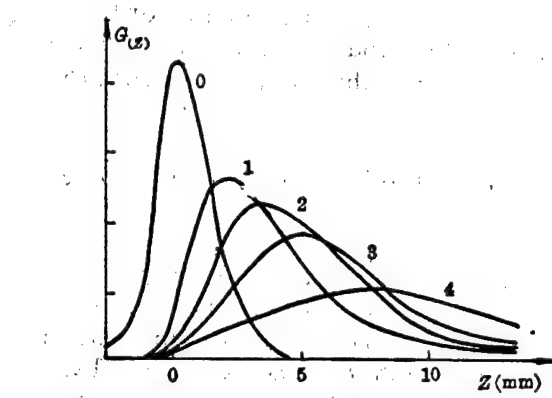


Figure 2. Atomic Distribution in the z Direction

0--original distribution

1-- $f = 0.15$

2-- $f = 0.24$

3-- $f = 0.39$

4-- $f = 0.55$

$$j(v) = \frac{2}{A} \left(\frac{v}{A} \right)^3 \exp \left(-\frac{v^2}{A^2} \right) \quad (7)$$

here $A = (2kT/m)^{1/2}$, and substitute into Equation (6), we obtain the z distribution of the deflected atoms shown in Figure 4. The computed results show a greater fraction of atoms with a large deflection than is actually measured.

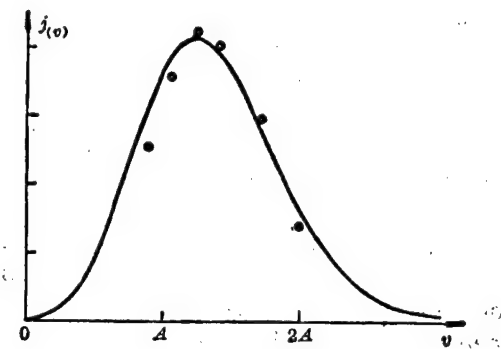


Figure 3. Atomic Velocity Distribution

The solid curve is the theoretical velocity distribution function and the circles are the experimental data.

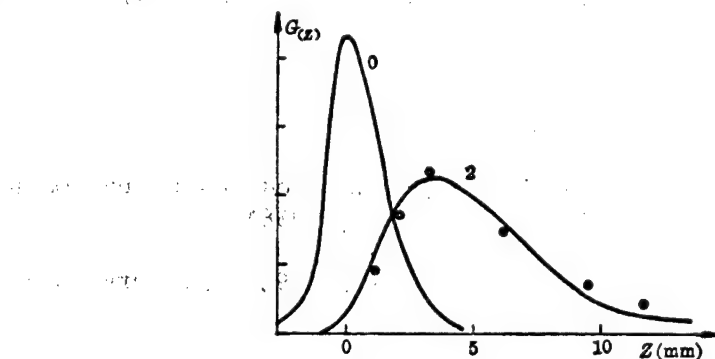


Figure 4. Comparison of Atomic Distribution in the z direction. The circles are theoretical values.

IV. Discussion

Experiments show that the atomic velocity distribution may be measured with the resonant light pressure deflection method. In particular, this method gives better results for atoms with a velocity greater than $(2kT/m)^{1/2}$. In our experiment, the measured deflection is 7.74 mm, which is the greatest deflection

measured in similar experiments. This shows that multiple light beam deflection of atomic beams is an effective tool for spectroscopic studies and for isotope separation. In the course of the deflection experiment, the velocity distribution parameters may be easily obtained as well.

In the velocity distribution measurement using resonant light pressure, there are three main sources of measurement error:

1. When the atomic beam is deflected, the flight direction is no longer rigorously perpendicular to the laser beam. Due to Doppler shift, the frequency detune increases. This effect is more pronounced for slower atoms with a greater deflection angle, causing them to fail to reach the expected deflection or decreasing the excitation probability in the detection. In any case, some of the slow atoms may be missed in the deduction of the velocity distribution function from the measured fluorescence intensity. This error may be reduced by increasing the laser power so that the saturation parameter becomes $S \gg 1$ and the atomic absorption line width $\Delta_{v_N} \sqrt{1 + S}$ is increased.
2. Equation (6) takes into account the original atomic distribution $F(z)$ of the beam but neglects the initial divergence angle of the beam. A simple analysis shows that the flight direction should be the sum of the initial divergence angle and the deflection angle. Therefore, Equation (6) may lead to relatively large error if the divergence angle is large.
3. Frequency instability of the laser causes fluctuation of the f value and directly affects the atomic distribution in z direction.

The authors thank Zhou Rufang [0719 3067 2658], Zhao Jiaming [6392 1367 6900], Ni Guoquan [0242 0948 2938], and Wang Changsheng [3769 7022 3932] for their assistance.

REFERENCES

1. Toennies, J.P., "In Chemische Elementarprozesse," ed. by H. Hartmann (Springer-Verlag, Berlin, Heidelberg, New York, 1968).
2. Gordom, R.J., et al., J. CHEM. PHYS., 1971, 54, 2393. K. Bergmann; APPL. PHYS., 1975, 8.65.
3. Wang Yuzhu, et al., ZHONGGUO KEXUE [CHINESE SCIENCE], (A), 1984, No 5, 467.
4. Citren, M.L., PHYS. REV., 1977, A16, 1507. V.I. Balykin, et al., JOURNAL OF EXPERIMENTAL AND THEORETICAL PHYSICS, 1979, 29, 614.

9698/9365
CSO: 4008/21

NUCLEAR DESIGN FOR QINSHAN 300 MWe PWR POWER PLANT

Beijing HE KEXUE YU GONGCHENG [CHINESE JOURNAL OF NUCLEAR SCIENCE AND ENGINEERING] in Chinese Vol 5 No 2, Jun 85 pp 104-113

[Article by Tang Bowen [0781 0130 3834] and Zhang Yongqian [1728 3057 6929] of the 728th Engineering Research and Design Institute]

[Text] I. Nuclear Design Task and Design Guidelines

The basic task of nuclear design is to ensure the operational safety of the reactor in terms of its nuclear characteristics and to satisfy the requirements of power generation and the specified design life of the power plant. Within the constraints of practical feasibility, the design goal is to flatten the power distribution as much as possible, to increase the average power density of the reactor core, to utilize nuclear fuel efficiently, to increase the burnout depth, to consider the adaptability of power plant operation, and to improve the economic performance of the power plant. At the same time, sufficient reserve capability must be provided to cover possible unexpected operating conditions. The nuclear design guidelines are:

1. The coefficient of power nonuniformity and the nuclear enthalpy rise factor of the reactor core under specified power output should not exceed the values as required by safety considerations.
2. The reactor core should have self-stability and controllability of Xenon oscillation.
3. The necessary cold-state and hot-state depth of reactor shut-down must be ensured.
4. The maximum speed of reactivity initialization must be limited.
5. The requirements on average burnout depth and the constraint on maximum burnout depth must be satisfied.

II. Development of Computer Programs for Core Physics Calculations

On the basis of the special features of the pressurized-water reactor, it is common practice to use a combined multigroup energy spectrum method and minor

group spatial diffusion method to develop assorted physics calculation programs. The so-called assorted programs are designed to accomplish the following tasks: 1) to perform the assorted calculations of the physical parameters specifically for design of nuclear power plants; 2) to provide different options of computational complexity which corresponds to the requirements of different stages of design: simplified computation, normal computation, and precision computation.

1. Development of Computer Programs for Core Physics Calculations at the 728 Research and Design Institute

To meet design needs, we have developed a preliminary set of assorted programs for performing physics calculations. For example, in the calculation of energy spectrum, we use a B_1 approximation fast neutron energy spectrum program to calculate the 68 group microscopic cross sections of various isotopes of the reactor core, and merge them into fast group and super-thermal group constants; we also use the thermal neutron Monte Carlo program to calculate the 66 group thermal neutron energy spectrum, and merge them into thermal group constants; to allow the calculation of nonuniform dense grid, we have developed a Monte-Carlo program for computing resonance spectrum; to simplify energy spectrum calculations, we have also developed an energy spectrum program based on collision probabilities. In spatial critical burnout calculations, we have developed minor group neutron diffusion finite difference programs for two-dimensional (XY), cylindrical (RZ), and axially-symmetric one-dimensional (Z) geometries, as well as two-dimensional and three-dimensional minor group node-block spatial burn-out programs. In addition to the above multifunction programs, we have developed special-purpose programs such as the programs for analyzing Xenon oscillation, for calculating β_{eff} , reactive temperature coefficient, the intensity of startup neutron source, and for analyzing reactive transient breakdowns. Also, we have developed a minor group three-dimensional neutron diffusion finite difference program used for validation purposes. There are a total of more than 20 computer programs.

2. Validation of Core Physics Calculations

In order to ensure the computational accuracy of the programs and the reliability of the computed design parameters, the programs were validated by comparing with published experimental results and calculated results from other programs; a large number of validation computations have also been made for the basic routines by using measured results from the zero-power reactor of a simulated PWR power plant. The validated parameters include critical K_{eff} , power distribution, the value of control rod, the value of boron, and the value of solid burnable poison and its effect on power distribution, the temperature reactivity coefficient, and the intensity of startup neutron source obtained from more than 60 different experiments. The calculated critical K_{eff} deviates from the experimental values by less than ± 1 percent with a relative standard deviation of $\sigma = \pm 0.72$ percent. The validation results of core power distribution indicate that the theoretically predicted hot spots and the position of the nuclear heat tube are in complete agreement with experimental results; the corresponding coefficient of power nonuniformity F_q^N and the nuclear enthalpy

rise factor $F_{\Delta H}^N$ differ from experimental results by less than ± 5 percent. If measurement errors are also taken into account, then the errors of F_q^N and $F_{\Delta H}^N$ would be less than ± 10 percent. Comparisons with the measured temperature coefficients of the zero-power reactor at low temperatures (10° - 70° C) and the intensity of startup neutron source show that the errors are within the allowable design tolerances.

In order to verify the reliability of the calculated hot-state full-power operating parameters of the reactor, we have performed calculations of the operating burnout parameters such as K_{eff} , power distribution, the yield of fission products, the burnout of burnable poison, and the final burnout life, etc.; the results show that the deviations are all within the limits of design tolerances.

From these validation calculations, we know that the accuracies of the important parameters for PWR power plant design such as critical K_{eff} , power distribution (F_q^N , $F_{\Delta H}^N$), burnout life, etc. calculated by the basic programs of the 728 Institute all meet the specifications of the 1971 IAEA Special Conference, as shown in Table 1.

Table 1.

Item	Validation error for room temperature zero-power reactor	Validation error for operating reactor	Computational error based on 1971 IAEA specifications
Effective multiplication coefficient K_{eff}	$\leq \pm 0.72$	$< \pm 0.25$	± 1
Coefficient of nuclear power nonuniformity F_q^N	$< \pm 10$	--	$\pm 8 - \pm 13$
Nuclear enthalpy rise factor $F_{\Delta H}^N$	$< \pm 10$	$\leq \pm 3.4$	$\pm 6 - \pm 13$
Life of reactivity	--	$\leq \pm 2.3$	$\pm 2 - \pm 10$

III. Nuclear Design for the Qinshan 300 MWe Power Plant

By reviewing foreign development in PWR technology and taking into consideration China's present conditions, we have completed the nuclear design for the Qinshan power plant. Table 2 presents the major physical parameters of the reactor core of the Qinshan power plant as well as the parameters of power plants of similar size in other countries. Figure 1 shows a diagram of the partitioning of the reactor core, the arrangement of burnable poison, and the grouping of control rods of the Qinshan power plant.

Table 2. Comparison of Major Performance Parameters of the Qinshan 300 MWe PWR Power Plant With Reactor Cores of Similar Size in Other Countries

Power plant	Qinshan 300 MWe	Sanonofre-1	Benzau-1	Mihama-1	R.E. Ginna	Tri-astin
Country	China	United States	Switzerland	Japan	United States	France
Date of operation	1966(1035)*	1968.1	1969.9	1970.11	1970	1979
Power MW	966(1030)*	1347	1130	1030	1300	2775
Electric power MW	300(330)*	430	364	320	470	966
Core dimensions D _c x H _c m	2.486 x 2.90	2.82 x 3.05	2.45 x 3.05	2.47 x 3.05	2.45 x 3.66	3.04 x 3.66
Partitioned fuel concentration	40.75	65.3	45.8	45	54.9	72.5
Number of reactor core fuel components	2.4/2.672/3.0	3.15/3.40/3.85	2.4/2.8/3.5	2.27/3.03/3.40	2.44/2.78/3.0	1.8/2.4/3.1
UO ₂ loading	121	157	121	121	121	157
Partitioned fuel concentration mm	10	10.72	10.72	10.72	10.72	9.5
Fuel rod diameter V_{u0}/V_{u02}	2.065	1.67			1.83	1.98
K _{eff} (initial, cold-state, net)	1.269	1.254	1.72			
No. of control rod bundles (long/short)	37	45	29/4	29/4	29/4	48
Total control rod value	9.02	~7		7.4	6.8	9.7
Number of pieces of burnable poison	576	None	None	696	528	
$F_{\frac{1}{2}}^n / F_{\frac{1}{2}}^n$	3.02/2.90	3.23/3.11	3.25/	3.25/3.13	3.38/3.28	2.35/2.29
$F_{\frac{1}{2}}^n / F_{\frac{1}{2}}^n$	1.80/1.67	1.88/1.75	1.88/	1.88/1.75	1.77/1.75	
Volume power density (maximum/average) kw/ft^3	206.9/68.6 (22.7/73.5)*	228.6/71.6	235.2/77.9	231.8/71.8	285/84.3	246.8/105
Line power density (maximum/average) kw/ft	12.4/4.11 (13.3/4.4)*	15.4/4.77	16.9/5.21	15.66/4.85	18.9/5.59	
Head furnace burnout concentration	MWd/tu	11900	13500		14900	
Balanced circulation burnout concentration	MWd/tu	30000	29500	27000	24400	33750
Moderator temperature coefficient $\times 10^{-4}/^{\circ}\text{C}$	0-6.0	+1.8--6.3		-1.3--7.6	+0.9--6.3	-0.5--7.0

*the numbers in parentheses are design values for reinforced conditions, see Reference 2 for details. Other parameters of the Qinshan reactor are: thermal neutron flux (maximum/average) $1.08 \times 10^{14} (1.16 \times 10^{14})/3.86 \times 10^{13} (4.14 \times 10^{13}) \text{ n/cm}^2 \cdot \text{s}$; initial net hot-state full-power critical boron concentration 4.152 ppm; reactivity of burnable poison (cold-hot) 6.03/7.12; Toepler coefficient -2 to -3.6 $\times 10^{-5}/^{\circ}\text{C}$.

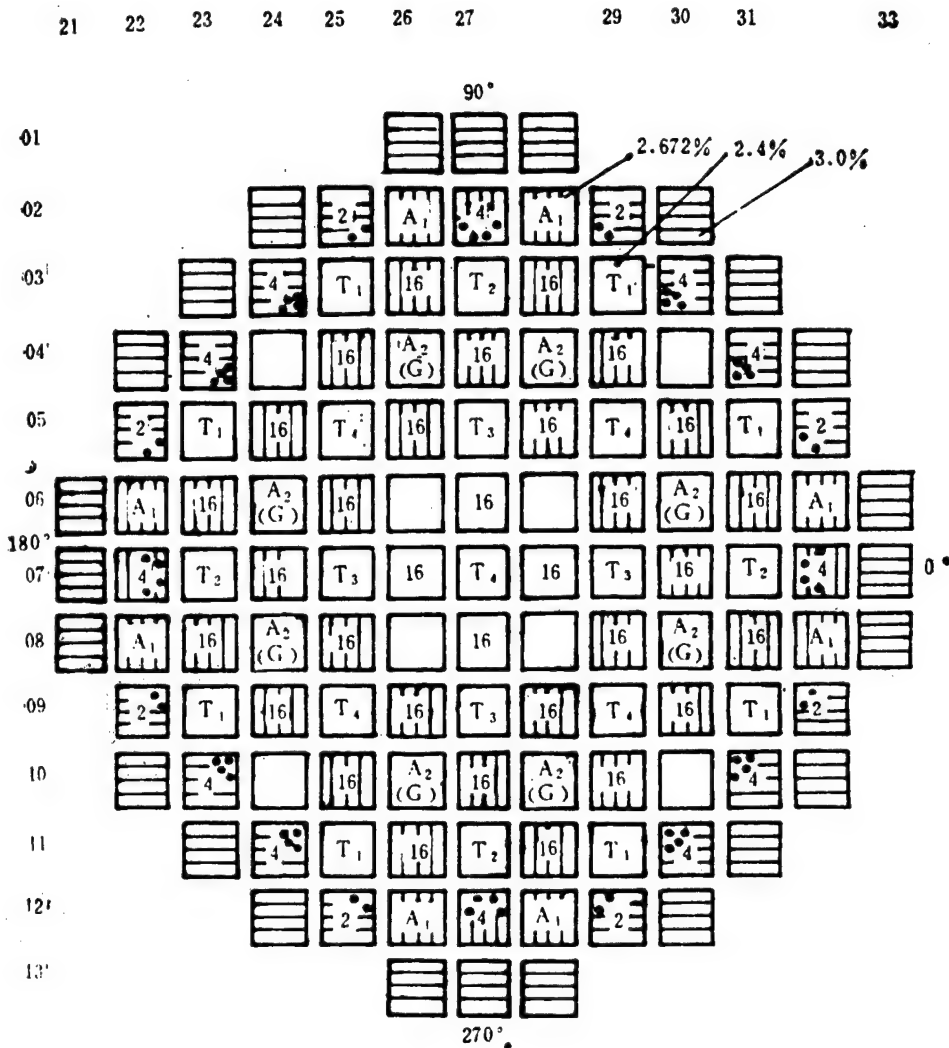


Figure 1. Arrangement of Reactor Core of Qinshan Nuclear Power Plant

1. The numbers in the figure represent the number of pieces of burnable poison, total number 576
2. The symbol • represents the position of burnable poison in the peripheral components of the reactor core
3. Safety rods: A₁ 8 bundles, A₂ (including power rods G) 8 bundles
4. Regulating rods: T₁ 8 bundles, T₂ 4 bundles, T₃ 4 bundles, T₄ 5 bundles

3.1. Selection of Reactor Core Grid Parameters

The discussion here will be limited to the selection of a few important parameters.

1. Relation between water-uranium ratio of fuel grid element V_{H_2O}/V_{UO_2} and burnout depth. A peak value of burnout depth exists in the vicinity of $V_{H_2O}/V_{UO_2} \geq 2$, and within a certain range the burnout conversion ratio decreases monotonically with increasing V_{H_2O}/V_{UO_2} . Therefore, the water-uranium ratios of early designs of PWR's were smaller than 2 (see Table 2); the water-uranium ratio of current designs is slightly larger than 2 to allow more complete burning of the fissionable fuel without having to post-process the residues. The water-uranium ratio we selected is 2.065.

2. Selection of fuel rod diameter. From the point of view of thermodynamic heat transfer and safety considerations, a small rod diameter is more desirable because it reduces line power density and fuel temperature at the center. From the structural point of view, a large rod diameter is more desirable because it improves structural strength and stability, and increases productivity. From the physics point of view, a larger rod diameter provides higher loading, and increases the burnout life and burnout depth. On the basis of these considerations, we have chosen the fuel rod diameter to be 10 mm. In other countries, the Westinghouse Co. reduced the rod diameter from 10.72 mm to 9.5 mm to guard against possible breakdown due to loss of water; the GE Co. used a 9.7 mm fuel rod; however, the West German Union of Power Stations (KW-U) maintained a 10.75 mm rod diameter until the late 1970's.^{3,4} The purpose of reducing the fuel rod diameter is to lower the maximum line power density of the reactor core P_{l}^{MAX} ; as long as P_{l}^{MAX} of the PWR is less than the limiting line power density of 18 kw/ft (591 w/cm) which is imposed on the fuel enclosure by loss-of-water considerations, it should be much smaller than the line power density of 765 w/cm required to melt the reactor core.³ Therefore, in terms of the practical design of reactor core, a choice of rod diameter in the range of 9.5 - 10.75 mm is still quite safe. However, in view of the recent development to increase the water-uranium ratio in nuclear design (including KW-U0) there is again a trend to reduce the rod diameter.^{5,6}

3. Selection of fuel concentration. This primarily refers to selection of the balanced circulation U-235 concentration. For a PWR, the key parameter is the limiting burnout depth which the fuel rod can withstand; to determine the balanced circulation fuel depth based on the achievable burnout depth reduces the cost of power generation. For PWR's in existing power plants with capacity of 300 MWe or higher, the average burnout depth is in the 30,000-35,000 MMWe/tU range, and the corresponding balanced circulation fuel concentration is in the 3-4 percent range. The balanced circulation burnout depth of the Qinshan power plant listed in Table 2 is based on a concentration of 3.4 percent.

4. Selection of the height-diameter ratio of the reactor core. From the physics point of view the core should be as close to a right cylinder as possible. If the thermodynamic effect of reactor core heat transfer is

taken into consideration, the height-diameter ratio of PWR generally should be in the 1.05-1.2 range.

It can be seen from Table 2 that the water-uranium ratio, the balanced circulation fuel concentration, and the height-diameter ratio of the Qinshan power plant are quite reasonable; the fuel rod diameter is chosen to be on the safe side in terms of conditions in the early 1970's. It should also be pointed out that after completion of the power plant, the balanced circulation fuel concentration can be properly adjusted based on the fuel circulation cost, the tolerable burnout depth as well as the experience in fuel management.

3.2 Analysis of Reactor Core Power Distribution

The objective of power distribution analysis is to explore all possible measures to flatten the power distribution, raise the average power density, increase the reactor output and reduce the cost per unit power generated by the power plant. It is well known that the key indices for evaluating the reactor core power distribution are the coefficient of nonuniformity F_q^N and the nuclear enthalpy rise factor $F_{\Delta H}^N$, which are defined as follows:

$$F_q^N = \frac{\text{maximum line power density}}{\text{reactor core average line power density}} = \frac{P_1^{\max}}{P_1}$$

$$F_{\Delta H}^N = \frac{\text{maximum temperature fuel rod power}}{\text{reactor core average fuel rod power}} = \frac{P_T^{\max}}{P_T}$$

Carrying out the three-dimensional integrated calculations, they can be expressed as:

$$F_q^N = \max[F_x, F_t, F_z] F_q^C F_q^U \quad (1)$$

$$F_{\Delta H}^N = \max[F_x, F_t, \frac{1}{H_c} \int_0^{H_c} F_z(z) dz] F_{\Delta H}^C F_{\Delta H}^U \quad (2)$$

where F_{xy} is the planar (radial) power distribution factor, F_z is the axial power distribution factor, F_q^C and $F_{\Delta H}^C$ are respectively the correction factors to account for effects not considered in the three-dimensional model such as the effects of control rod pull-out and temperature feedback; F_q^U and $F_{\Delta H}^U$ are respectively the computational error of F_q^N and $F_{\Delta H}^N$; H_c is the height of the reactor core.

There are many factors in a PWR that affect the power distribution. In a general sense, the planar power distribution is determined by the partitioning of fuel concentration, the arrangement of burnable poison, the grouping and the pull-out sequence of the control rods. The local power distribution inside the fuel component is affected by its composition and arrangement, particularly by the presence of water holes. The axial power distribution is determined by such factors as the form of control (the grouping of control rods, the pull-out sequence, and the selection of the regulation band), the

axial dimension and arrangement of fuel component frame structure, the height of reactor core and the effect of temperature feedback.

It should be pointed out that the design specification of the coefficient of power nonuniformity is in general determined by the reactor core and the initial power distribution. As the burnout depth increases, the power distribution becomes more uniform; hence, one of the most important tasks in nuclear design is to flatten the initial power distribution of the reactor core and to determine the coefficient of power nonuniformity. Of course, it is also important to make predictions of the power distribution over the burnout life.

We shall now briefly discuss the effect of using burnable poison to flatten the power distribution and the effect of different forms of rod control on the power distribution.

We have adopted the experience of other countries to improve the arrangement of burnable poison by moving the burnable poison from the peripheral components toward the center of the reactor core, thereby removing the part of burnable poison which caused the power to be suppressed (indicated by "•" in Figure 2); as a result, the power distribution is improved, its coefficient of planar power nonuniformity is $F_{xy} = 1.266$ (Figure 2). Figure 3 shows the planar power distribution located at the main regulating rod assembly T_4 . Also, based on our own experience, we found that by shortening the axial dimension of the burnout poison, and using a nonsymmetric arrangement, the axial power distribution can also be flattened. This finding has been incorporated in the design of the Qinshan power plant.

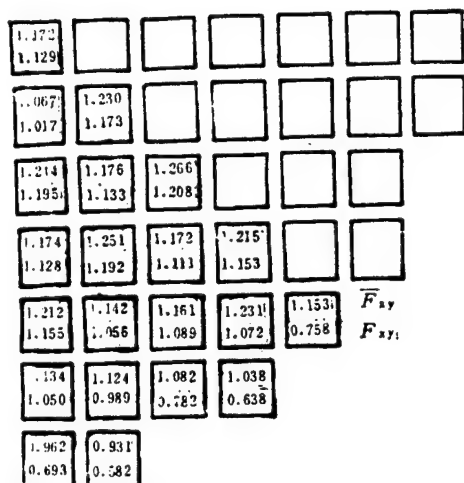


Figure 2. Planar Power Distribution Flattened by Rearranging Burnable Poison

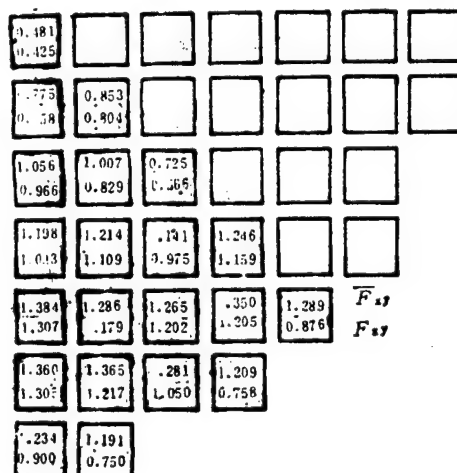


Figure 3. Planar Power Distribution at Main Regulating Rod Assembly T_4

However, the main factor which affects the axial power distribution of the reactor core is the selection of the form of rod control. In PWR's designed in the 1960's, the majority of regulating rods used were large-value control rods, which caused excessive distortions in the axial power distribution; subsequently, they were replaced by small-value regulating rods and the rods were shortened, which greatly improved the axial power distribution. By the mid 1970's, it was discovered that leaving the short rods in the reactor core produced a screening effect on the fuel burnout, and excessive local power peaks were generated once the short rods were withdrawn. For this reason, the short rods were eliminated. In order to coordinate between load regulation and the control of power distribution (including control of Xenon oscillation), we have proposed an improved form of rod control; the corresponding control rod assembly and the pullout sequence are shown in Figure 1 and Figure 4, respectively. In this design, a power distribution control rod assembly G with a 2 percent value is sufficient to control Xenon oscillation, and a rod assembly with a 1 percent value is used for load regulation, the other rod assemblies are safety rods. Also, during the initial and middle stages of burnout of the 300 MWe reactor, no Xenon oscillation will occur, hence the G rod assembly is not inserted into the reactor core. Within the commonly used regulation band of power plant reactors (rod assembly integrated value 0.2 percent - 0.5 percent), this improved form of rod control can reduce the coefficient of power nonuniformity by at least 10 percent compared to the L rod plus D rod control of the West German KWU (the L rod value is approximately 5 percent - 6 percent).

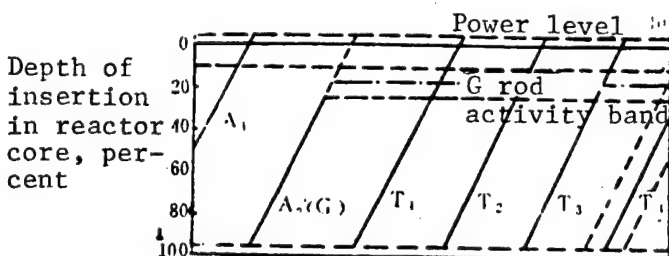


Figure 4. Rod Pullout Sequence

After measures are taken to flatten the power distribution, the coefficient of power nonuniformity and the enthalpy rise factor can be calculated from equations (1) and (2), and the results are presented in Table 3. It is seen that the design coefficient of power nonuniformity F_q^N of the Qinshan reactor core including 10 percent computational error can be as large as 2.5 (the values $F_q^N \leq 2.90$, $F_{\Delta H}^N \leq 1.67$ listed in Table 1 and Table 2 are design specifications for the reactor core of the Qinshan power plant).

Table 3. Design Coefficients of Nuclear Power Nonuniformity of the Qinshan Power Plant Reactor Core

F_1	F_2	$F_q^c / F_{\Delta H}^c$	$F_q^u / F_{\Delta H}^u$	F_q^u	$F_{\Delta H}^u$
1.266	1.080	1.646	1.007/1.03	1.1/1.1	2.50

$$\cdot F_q^c = F_q^{\text{失步}} \cdot F_q^{\text{格架}} \cdot F_q^{\text{温反馈}}, \quad F_{\Delta H}^c = F_{\Delta H}^{\text{失步}}$$

3.3 Reactor Core Burnout Analysis and Fuel Management

Here, we shall briefly discuss the form of fuel loading and replacement; for a detailed discussion see Reference 8.

With the exception of Rengel,⁹ who used the single-sector fuel loading technique, and Stade,¹⁰ who used the four-sector fuel loading technique, almost all power plant PWR's use the three-sector fuel loading technique and the batch fuel replacement procedure. The main reasons for choosing this technique are as follows:

1. Flattening the power distribution. The coefficients of planar power non-uniformity for three-sector loading (2.3 percent, 2.7 percent, 3 percent) and single-sector loading (2.7 percent) are, respectively, 1.33 and 1.84; a difference of 28 percent.
2. Increasing the burnout depth. It can be seen from Table 4 that the residue burnout depth for three-sector, three-batch fuel replacement is almost double that for single-batch replacement; as a result, the utilization rate of U-235 is increased by 14.6 percent.

Table 4. Comparison of Three-Sector Batch Replacement and Single-Batch Fuel Replacement

Fuel replacement procedure	Single-batch fuel-replacement	Three-sector, three-batch fuel replacement
Added fuel concentration from fuel replacement, percent	2.4, 2.7, 3.0	3.0
Added amount of U-235 from each batch of fuel replacement, kg	971	356
Amount of U-235 residue removed from each batch of replaced fuel, kg	505	133
Residue burnout depth, MWd/tU	12,300	25,000
U-235 utilization rate, percent	48	62.6

The Qinshan power plant also uses the three-sector fuel loading and replacement procedure (see Figure 2). In order to reduce the cost of power generation, we have recently changed the balanced circulation fuel concentration from 3 percent⁸ to 3.4 percent, and the corresponding burnout depth has increased from approximately 25,000 MWD/tU to 30,000 MWD/tU.

However, in the 1980's, a new low-leakage fuel replacement technique which loads the fuel into the inner core region has been developed. Of course, we shall use this technique for fuel management of the Qinshan power plant. If in addition we use an all-zirconium reactor core and keep the balanced fuel concentration at 3.4 percent, then the burnout depth can be expected to exceed 33,000 MWD/tU.

3.4 Control of Reactivity

In order to increase burnout life, the initial fuel loading of the PWR core has very high reserve reactivity, its cold-state net K_{eff} can reach 1.25-1.30. Therefore, early 300-MWe PWR's such as the Obrigheim used a control technique consisting of both chemical poison (boric acid) and control rods; the initial critical boron concentration was as high as 1,700 ppm, and the moderator temperature coefficient became positive, which caused a great deal of control rod activities during operation.¹¹ Later, a design rule was imposed that the moderator temperature coefficient cannot be positive during heat-power operation, and solid burnable poison was used in place of liquid boron for controlling part of the reactivity.

1. Control of chemical poison. Uniformly distributed chemical poison in the reactor core does not perturb the power distribution. But since the regulation of boron concentration is very slow, it is generally used to control slowly-varying effects of reactivity such as the temperature effect of changing from cold-state zero power to hot-state zero power, the accumulated effect of fuel burnout and fission products, the burnout compensation of burnable poison, the poisonous effect of balanced xenon and samarium, and cold-state shutdown depth and fuel replacement shutdown depth.

2. Control of rod bundles. The higher speed of rod control can cause distortions in the power distribution of reactor core; it is generally used to control rapid changes in reactivity. They include: the temperature effect of moderator within the hot-state power range and the fuel Toepler effect, the effect of power redistribution, the bubble effect, and the hot-state shutdown path.

The amount of solid burnable poison should be chosen such that no positive moderator temperature coefficient will appear under hot-state zero-power conditions. In the final stage of burnout, the burnable poison should be completely burned up to avoid burnout suppression.

The total number of control rods (total value) is determined by safety considerations of a hot-state shutdown. The required rod-control reactivity of a PWR is highest in the final stage of balanced circulation, but the total value of rod-control at this time is smallest. Therefore, safety considerations dictate

that the total number of control rods should be determined in the final stage of balanced circulation. Generally speaking, the total value of control rods in the initial stage should be > 9 percent. The corresponding number of control rod bundles in the reactor core should be approximately one-third the number of fuel components. The maximum speed of reactivity initialization should be constrained in the pullout sequence. The rod control capability of the Qinshan power plant satisfies all these design requirements (see Table 2).

In addition, we also considered temperature effect compensation by using coolant to improve the power recovery capability under changing operating conditions of the power plant (particularly in the later stages of burnout).

Based on the above analyses and comparisons, it can be stated that the design of the Qinshan 300MWe PWR power plant not only had incorporated the design experiences of early PWR's of similar size, but had also taken advantage of the experiences of more recent large-scale PWR's. Our design calculations were sufficiently validated, and the final design is considered reasonable and consistent with the basic ground rules of nuclear design with adequate margin in safety and controllability of the reactor core.

REFERENCES

1. CONF-73414-p2, VII-39 (1971).
2. Ou-Yang Yu, CHINESE JOURNAL OF NUCLEAR SCIENCE AND ENGINEERING, Vol 3 No 1, pp 1-10 (1983).
3. Markl, H., Core Engineering and Performance of KWU Pressurized Water Reactor, Reactor Systems Engineering Division, Kraftwerk Union Aktiegesellschaft (KWU), Erlangen, February (1976).
4. Bevilacqua, F., System 80: Combustion Engineering Standard 3800 MWt PWR, Proceedings of the American Power Conference, Vol 36 (1974).
5. Kraftwerk Union, 1,000 MWe Pressurized Water Reactor Nuclear Power Plant, April (1984).
6. Westinghouse Proposal for a 1,000 MWe Standard Nuclear Power Plant Vol 3 (1984).
7. Tang Bowan, Weng Yenfeng, and Ye Shimin, "Investigation of PWR Rod Control for Nuclear Power Plants."
8. Li Huizhu, Ye Shimin, and Xu Weizu, CHINESE JOURNAL OF NUCLEAR SCIENCE AND ENGINEERING, Vol 1 No 1, pp 28-36 (1981).
9. Rengel, J.C. and Johnson, W.E., PROC. 3d Intern. Conf. Peaceful Uses of Atomic Energy, Geneva, p 203 (1964).

10. Atomwirtschaft-Atomtechnik, Stade (KKS) No 11 (1971).
11. 4th Intern. Conf. on the Peaceful Uses of Atomic Energy, Vol II,
p 806.

3012/9365
CSO: 4008/415

PROGRESS IN PLASMA FOCUS RESEARCH

Beijing HE KEXUE YU GONGCHENG [CHINESE JOURNAL OF NUCLEAR SCIENCE AND ENGINEERING] in Chinese Vol 5 No 2, Jun 85 pp 165-173

[Article by Yang Jinji [2799 3160 1015] and Han Min [7281 2549]]

[Text] Preface

It has been more than 20 years since Mather and Filippov developed plasma focus devices (abbreviated DPF) in the United States and the Soviet Union, respectively. From 1960 to 1962, Filippov converted the Z-pinched device into a flat-plate type device¹⁻² (see Figure 1a). During the same period, following the idea of a coaxial gun accelerator of Marshal and Ohser, Mather developed a coaxial type DPF device³⁻⁴ (see Figure 1b). Although these two devices have different structures, they have similar properties, and they constitute the two basic forms of DPF. Derived from these are the hypocycloidal-pinch type DPF, the staged DPF, and the cusp type DPF.

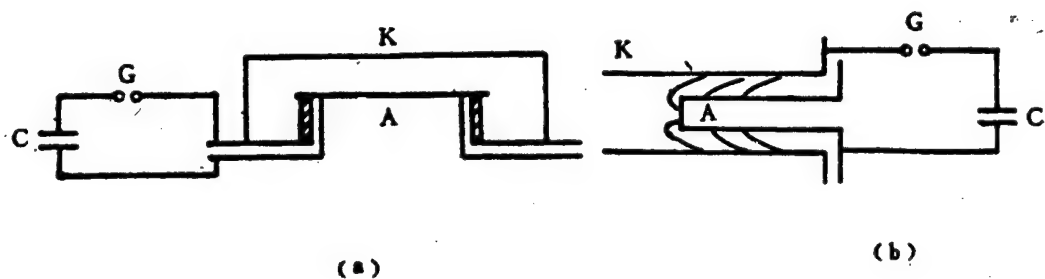


Figure 1.

Plasma focus has many applications: 1) applications in nuclear fusion such as the feasibility study of a mixed fission-fusion reactor,⁸ the idea of a reactor using ⁶LiD discharge,⁹ and the use of multichannel DPF bombardment to achieve fusion⁶; 2) pulsed radiation source for neutrons, particle beams, and X-rays; 3) simulation of nuclear weapons; 4) other applications such as trigger for iodine laser,¹³ vacuum ultraviolet radiation source,⁸ chip mask-making technology,¹⁴ etc. These applications have attracted the attention of many different countries; at present, there are approximately 40 DPF installations in the world.

China has also begun its DPF research, which includes the study of various engineering problems, and the problems of X-rays, neutron emissions, initial discharge, etc.¹⁵⁻¹⁷

I. Overview of Plasma Focus Research

It is known from experimental results that the number of neutrons produced by a DPF depends on the plasma current. Therefore, strong pulse neutrons can be obtained by increasing the current of the DPF.

In general, plasma focus devices use capacitors for energy storage, which range from 1 kJ to 1 MJ. For example, Italy has a 1 MJ device, Germany, the United States, and France have installations in the range of 340-500 kJ; Poland is in the process of constructing a 1 MJ installation.¹⁸⁻²² The parameters which are achievable today are as follows:

1. Neutrons. In a 500 kJ installation: 2.45 MeV neutrons, 6×10^{12} /pulse, 10^{11} n/cm² pulse. In the deuterium experiment, small quantities of D-T neutrons have been observed; the ratio of D-T to D-D neutron yield is $Y_{dt}/Y_{dd} = 6 \times 10^{-4}$. Cloth of Germany had proposed a 20 MJ design, and predicted D-T neutron level of 4×10^{17} n/pulse. The Lawrence Livermore Laboratory in the United States estimated that a 9 MJ device can achieve a level of 6.5×10^{18} n/pulse.

2. Electron Beam. The results from a 340 kJ device are presented in Table 1. The electron energy is 200-300 keV, the power is $(0.4-0.8) \times 10^{12}$ W. Nardi obtained electron beams from an emission source with power level of ≥ 1 TW/cm² pulse at 0.8 MA.

Table 1.

Electron energy keV	Energy of electron beam, kJ/pulse	Current of electron beam, MA
50	58	33
200	14.5	2
300	9.6	0.9

3. The deuteron parameters of an ion beam from a 340 kJ device are presented in Table 2. When the energy is 80-100 kJ, Steinmetz obtained the yield of D⁺ to be $(3.3-6) \times 10^{16}$ /pulse,²³ the D⁺ energy level can reach 6 MeV. In addition, O⁺ - O⁸⁺, N-N⁷⁺, C⁺ - C⁸⁺,²⁴ and Fe¹⁵⁺, Cu¹⁹⁺, Mo²⁰⁺, W²⁵⁺ plasma were also observed, the maximum energy level was as high as 1 MeV.²⁵

4. X-ray. Photon energy ranges from 1 to 200 keV, with a small fraction of photons reaching 1 MeV. In the 340 kJ device, yield levels of 150 J/pulse have been obtained. Experimental results show that the high energy photons depend on the material of the electrodes.

Table 2.

Ion energy keV	Energy of ion beam, kJ/pulse	Current of ion beam, MA
70	220	62
100	120	24
300	28	1.9

II. Selection of Device Parameters

The operation of a plasma focus device can be illustrated by using the example of Figure 1b. The fully charged capacitor C will discharge through the spark gap G toward the coaxial electrode A-K. Due to the effect of Lorentz force, the current layer S moves forward along the electrode; when it reaches the top of the anode A, the current layer contracts inward, and forms a focal point in front of the anode A. Its density is approximately 10^{19} cm^{-3} its temperature is 600-1,000 eV, and it emits neutrons, particle beams, and X-rays.

In order to increase the plasma current which affect the neutron yield, the device parameters must be properly selected; they include: 1) electric circuit parameters such as inductance, voltage, etc., 2) parameters of the discharge chamber such as the electrode dimensions and gas pressure.

The electric current is given by the following expressions

$$I = U \sqrt{\frac{C}{L_0}} \quad \text{or} \quad I = \sqrt{\frac{2W}{L_0}} \quad (1)$$

where U, C, L_0 , W are respectively the charging voltage, the capacitance, the inductance of the circuit, and the stored energy. Equation (1) shows that the electric current varies inversely with inductance, and does not seem to depend on voltage; but according to magneto-hydrodynamic calculations,²⁶ this assertion is not necessarily correct (see Table 3).

Table 3.

Case No	Stored energy W, kJ	Voltage U, kV	Inductance L_0 , nH	Plasma current I_p , kA	Neutron yield Y_n , 10^9 /pulse
1*	12	20	8.3	550	2.6
2*	12	20	2	570	3
3*	12	85	8.3	810	9.6

A comparison of case 2* (small inductance) and case 1* (large inductance) shows that the current does not increase according to the ratio $\sqrt{8.3/2}$; similarly, the current I_p is different for case 1* and case 3* where the inductances are equal. This illustrates the fact that reducing L_0 does not necessarily cause

I_p to increase. MHD calculations show that a proper design must take into consideration not only the circuit parameters but also parameters of the discharge chamber.

Attempts have been made to use the method of "similarity relation" to find the relationships between various parameters. It is based on the following idea: when the plasma reaches the center of the electrode terminal, the electric current also reaches maximum. In other words, the plasma will be focused under maximum current, hence maximum neutron emission is achieved. From this one obtains the "similarity relation" $I^2/(p_0 r_i^2) = \text{constant}$, where p_0 , r_i are respectively the gas pressure and the radius of the inner electrode. By using the circuit equations,²⁶ the optimum parameter values can be obtained.

$$\left. \begin{aligned} U_{0,0pt} &= 2.118 (WI_0 L^2)^{1/2} \\ I_{max,0pt} &= 0.639 \left(\frac{WI_0}{L} \right)^{1/3} \\ \tau_{0pt} &= 1.486 \left(\frac{W}{I_0^2 L} \right)^{1/3} \end{aligned} \right\} \quad (2)$$

where the notation (\cdot) indicates derivative with respect to time. While the MHD method is very useful, it involves tedious computations; consequently, the "similarity relation" is used only as an initial step in the design process.

In 1983, Decker proposed a new design²⁷ which differs from conventional devices. By using high voltage and large circuit inductance, he was able to achieve focusing efficiency (Y_n/W) 4 times larger than conventional devices. The basic idea is as follows: since the load (discharge) impedance Z_L is a variable, if the circuit impedance Z_0 is greater than Z_L most of the time, then there exists a high-voltage and short-duration "hard" power source which can produce very large input current. In 1983, Czekaj, et al.,²⁸ pointed out that the root structure of the electrode has a significant effect on neutron emission and X-rays. To understand how the discharge conditions are affected by the electrode structure and dimensions, the gas pressure and circuit parameters is a very complicated problem. It is a topic of current research to determine the optimum operating conditions.

III. Plasma Focus Discharge Process

In the early 1970's, knowledge of the plasma focus discharge process was rather crude. The development of new detection techniques such as laser diagnosis, high-speed photography, and soft X-rays provided a better understanding of the process of focus formation. According to the laser interferogram (see Figure 2),²⁹ the process of focus formation can be divided into five different stages. Let $t = 0$ be the time of maximum compression, then the five stages are: 1) the stage of plasma compression, $t < 0$ (Figure 2-1); 2) the stage of dense plasma, $t \approx 0$, in which the diameter of the focal point is smallest

(3-4 mm) and the plasma density is maximum ($\sim 10^{19} \text{ cm}^{-3}$); the soft X-rays become hard, and the temperature rises; 3) the first expansion stage, $50 \text{ ns} \gtrsim t \gtrsim 5 \text{ ns}$ (Figure 2,3-6), in which the diameter of the focal point increases to 8-10 mm, and the temperature and density both decrease; 4) the unstable stage, $20 \text{ ns} \leq t \leq 70 \text{ ns}$ (Figure 2-7), in which $m = 0$ instability of the plasma column takes place, the local temperature and density again increase, and neutrons and X-rays are emitted; 5) the second expansion stage, $t \geq 70 \text{ ns}$ (Figure 2-9), in which both the plasma temperature and density begin to drop, but strong neutron emission continues. After $t \geq 80 \text{ ns}$, the plasma collapses. The times and plasma parameters of each stage differ from one device to another, but the basic process is the same.

In 1982, based on the discoveries from an experimental study conducted on the new Poseidon installation at the Stuttgart IPF Research Institute, a new theory of plasma development was proposed (see Figure 3).^{30,31} After maximum compression, individual filaments are formed inside the plasma column, which has much higher density (n), temperature (T), electric field (E), and magnetic field (B) than the surrounding region. Furthermore, after $m = 0$ instability, "turbulent packet" begins to appear, its parameter values can be as high as $E = 26 \text{ MV/cm}$, $B = 1.1 \times 10^4 \text{ Tesla}$. The Schlieren diagram (Figure 4)³² clearly shows the presence of filaments in the plasma. The phenomenon of "turbulent packet" is deduced from numerical calculations, it has not been verified by experiment.

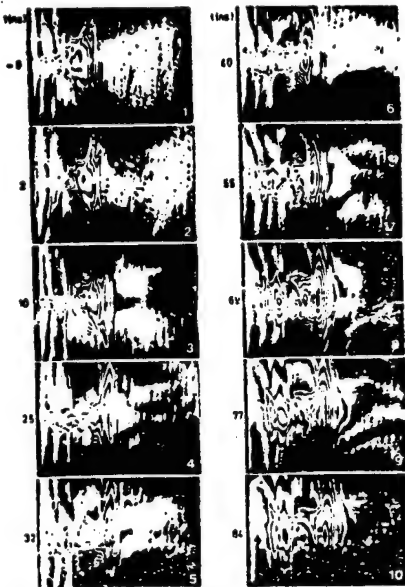


Figure 2.

60 KV 280 KJ 3 mb D₂ Y_N = 4.8 × 10¹⁰

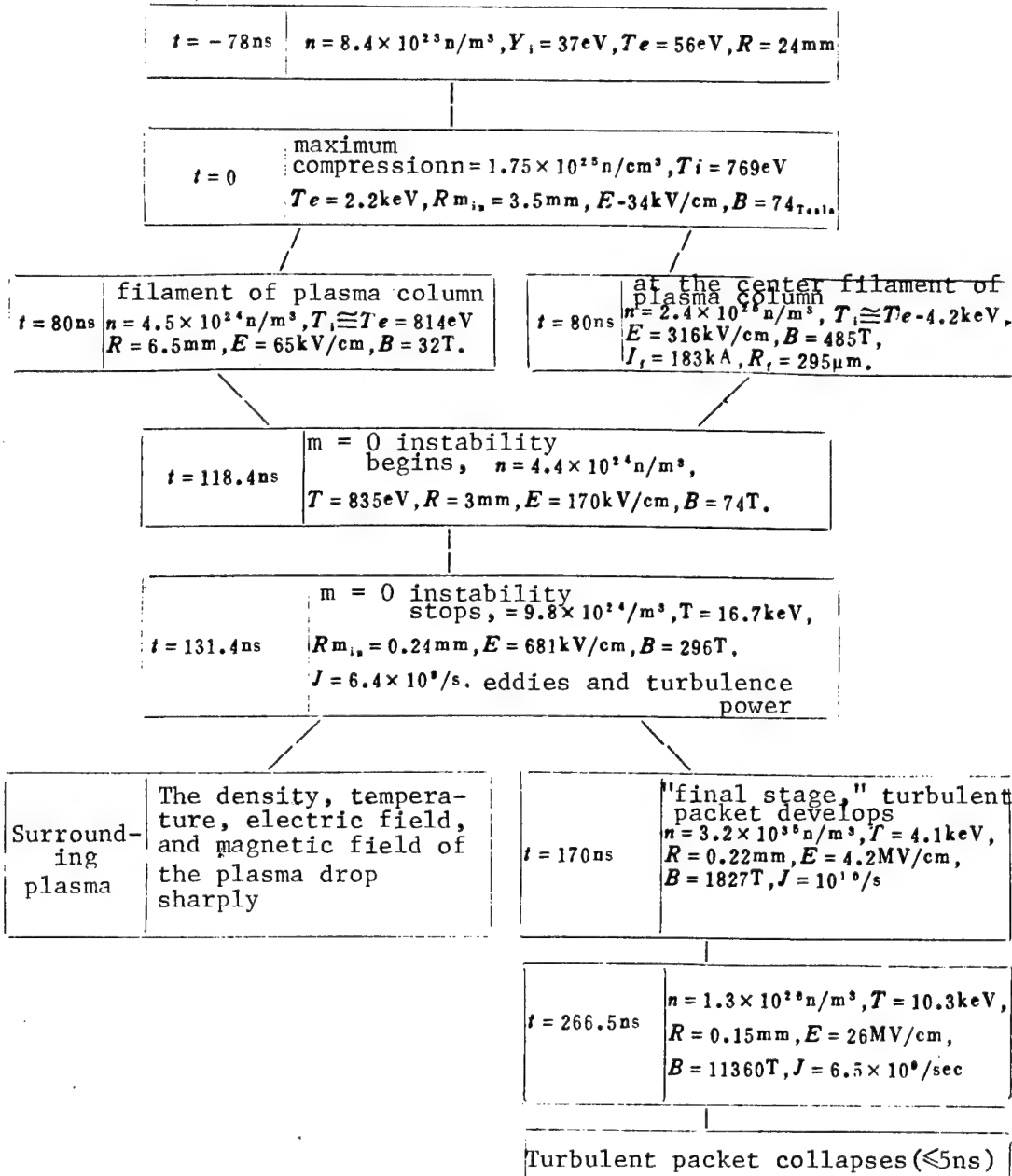


Figure 3. Block Diagram Showing the Plasma Development Process

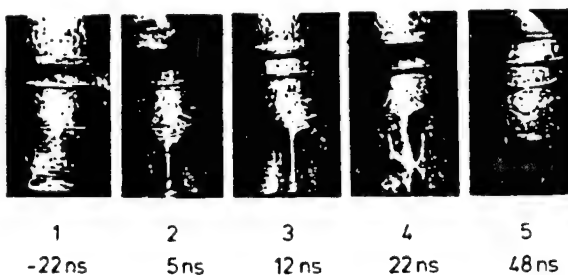


Figure 4.

IV. Emission of Neutrons

There are three aspects in the study of neutrons: 1) the mechanism of neutron production; 2) the problem of scaling law; and 3) the problem of nuclear fusion.

4.1 The Mechanism of Neutron Emission and the "Equilibrium Condition"

Based on experimental evidence, we know that the emission of neutrons is not isotropic, the peak of the neutron spectrum is not 2.45 MeV, and the neutron emission time is approximately 100 ns. To explain these phenomena, various models have been suggested such as the beam-target model, the beam-beam model, the moving furnace model, etc., but none of these models provides a completely satisfactory explanation.

In 1980, by using the neutron pin-hole method to determine the position of neutron emission and the neutron yield corresponding to different positions of emission,²³ it was found that approximately 65-80 percent of the neutrons are emitted from the neighborhood of the anode (< 5 cm), and they are approximately isotropic ($A = Y_{n-0^\circ}/Y_{n-90^\circ} \approx 1$). The neutrons farther away are produced by beam-target interaction; they are nonisotropic ($A > 1$).

A new discovery in 1982³³ showed that neutron emissions take place both before and after $m = 0$ instability (see Figure 5). According to theoretical analysis which takes into consideration the velocity v , the vortex $\varphi = \text{rot } v$, and the eddy current density (f) $\varphi_e = \text{rot } j$, current filaments exist in the middle stage (after maximum compression, but before $m = 0$ instability), and the local electric field propagates along the filaments, thereby accelerating D^+ , and causing D-D interactions to produce neutrons. The duration of this stage $\tau_{p3/2}$ increases with the plasma current I_p according to the relation $\tau_p \sim I_p$. The presence of filaments can also be seen in Figure 6,³⁴ represented by the D^+ traces perpendicular to the axial direction. After the decay of $m = 0$ instability, "turbulent packets" are formed in the plasma; both the magnetic and electric fields reach very high values, and neutrons are emitted. This process is almost independent of I_p . The filament-turbulence theory represents a major step forward in the development of neutron emission theory.

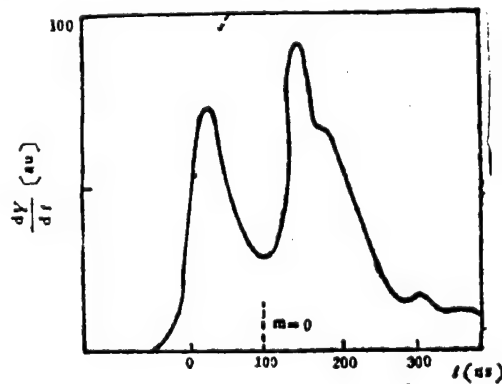


Figure 5.

The above discussion shows that in the middle stage of focus development, the plasma density is of the order of 10^{14} cm^{-3} , and its duration is $\tau \sim I_p^{3/2}$. It is conjectured that "equilibrium condition" will be reached at $I_p = 20 \text{ MA}$, when $\tau = 10 \text{ ns}$. Therefore, Herold had proposed the idea of using it as a fusion reactor.³³



Figure 6.

4.2 The Scaling Law of Neutron Emission

The neutron yield data obtained from the DPF devices of different countries can be combined into a curve (as shown in Figure 7) which followed the relationship

$$Y_n \sim I_p^m \quad \text{where } m = 3.3-4 \quad (3)$$

In a 1 KJ device, m may be even higher. This relationship can also be obtained theoretically. Y_n is proportional to the square of the deuteron density (n^2); but according to the Benett formula, $I_p \sim \sqrt{n}$, therefore,

$$Y_n \sim n^2 \sim I_p^4 \quad (4)$$

This scaling law is valid even in the newest neutron emission model.³³

V. Particle Beam

In the late 1970's, efforts were initiated to study the DPF emission of ion beam and electron beam. At present, most of the research work are concentrated on D^+ beams. The energy spectrum of D^+ particles is shown in Figure 8,³⁵ where Ω denotes the solid angle, and E_d is the energy of D^+ particles. The fact that the energy distribution depends on the gas pressure was pointed out by other researchers.^{36,37} The D^+ energy may be as high as 5.1 MeV, and the number of D^+ particles is $1.2 \times 10^{17} / \text{str}$.

The following facts should be pointed out with regard to the yield of ion beam (Y_d) and neutron yield (Y_n). The optimum conditions for Y_d and Y_n are different; generally, the gas pressure for optimum Y_d is lower than that for

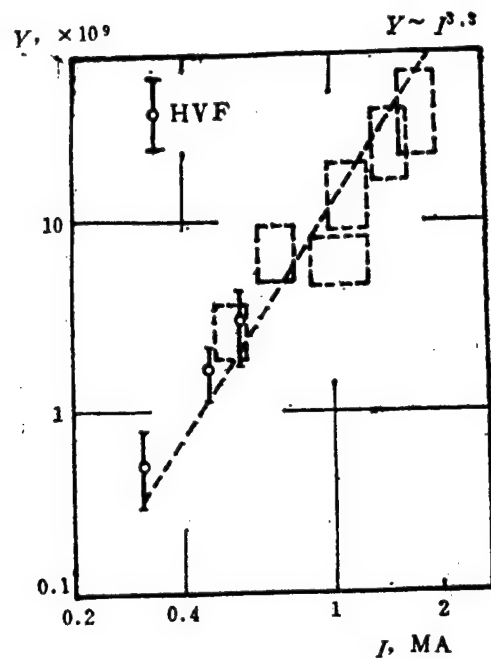


Figure 7.

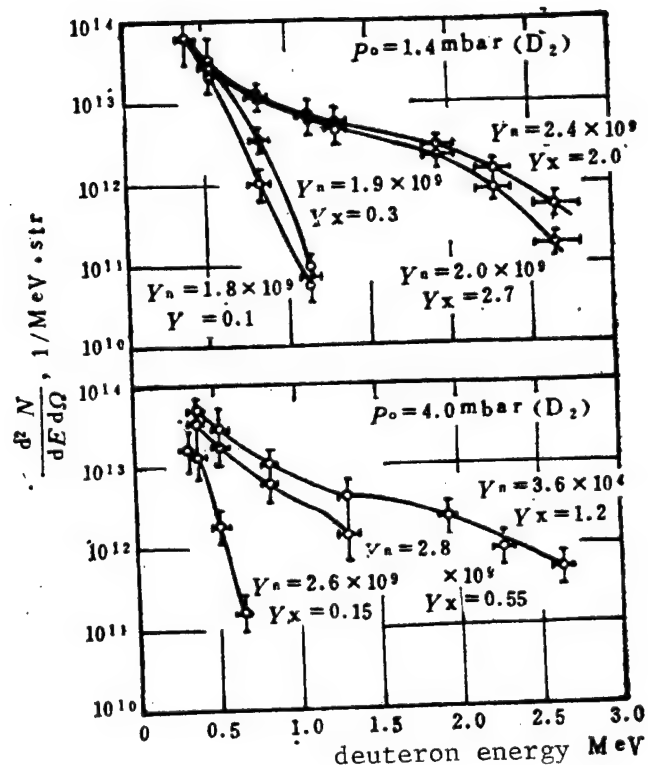


Figure 8.

optimum Y_n . Also, high-energy D^+ particles ($E_d \geq 350$ keV) have very little effect on Y_n (1 percent); only low-energy D^+ particles have significant effect on Y_n . Neutron pin-hole experiments^{34, 35} show that large D^+ sources (approximately several square mm) produce low-energy particles ($E_d < 2$ MeV), whereas a number of small D^+ sources produce high-energy D^+ (2 MeV $\leq E_d \leq 4.5$ MeV) particles. These experimental evidence provide valuable hints in trying to explain the mechanism of neutron emission because they are consistent with the turbulence and filament model.

In addition to D^+ , DPF can also produce O, N, C, Fe, Cu, Mo, and W plasma beams. By using modified structures, high-energy ion beams can be obtained³⁹; for example, the energy levels corresponding to ^{40}Ar , ^{56}Fe , ^{63}Cu , and ^{114}W are, respectively, 20 MeV, 70 MeV, 25 MeV, and 100 MeV. It was also found from experiment that the maximum energy E_{\max} of the accelerated ions is related to the electric charge Z as follows:

$$E_{\max}/Z = 1.8 - 1.9 \text{ MeV} \quad (5)$$

and that the energy distributions of different ions are similar. Therefore, it was thought that different types of ions are accelerated by the same process or in the same electric field.

In DPF, the electron beam is emitted in the opposite direction as the ion beam. Its energy level is generally several hundred keV; in a few cases it can reach 1 MeV. Figure 9 shows the energy distributions of electron beam and D^+ ⁴⁰; they both obey an exponential relation of the following form:

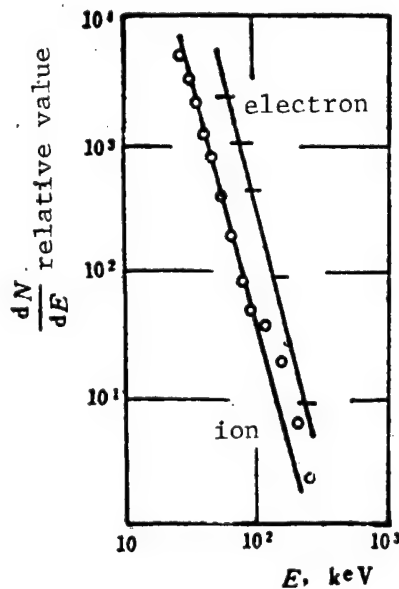


Figure 9.

$$\begin{aligned}\frac{dN_p}{dE_d} &\sim E_d^{-3.4 \pm 0.4} \\ \frac{dN_e}{dE_e} &\sim E_e^{-3.6 \pm 0.3}\end{aligned}\tag{6}$$

Therefore, it was thought that the D^+ beam and the electron beam may be produced by the same electric field. The yield of the electron beam is a function of the maximum discharge current

$$Y_e \sim I_m^{4.4 \pm 0.3}\tag{7}$$

VI. Concluding Remarks

After 20 years of DPF research, the understanding of its physical process has been significantly improved; also, new forms have been developed by combining it with Z-pinch, gas jet, internal explosion, etc. Future DPF research should cover the following areas: 1) plasma motion, and the mechanism of neutron and ion emission; 2) the scaling law between Y_n , its duration, and I_p ; 3) the use of DPF as the source for ion beams, electron beams, and X-rays; 4) the problem of mixed fusion-fission reactor; 5) the study of the parameters, structures, and types of optimum devices to meet different requirements for neutrons, ion beams, electron beams, and X-rays.

REFERENCES

1. Potrov, P.P., et al., "Plasma Phys. and Probl. Controlled Thermonucl. Reaction," Vol IV (1960).
2. Filippov, N.V., et al., NUCL. FUSION, SUPPL., Pt 2 (1962).
3. Marshall, J., PHYS. FLUIDS, 8, 134 (1960).
4. Mather, J.W., PHYS. FLUIDS, 7, 5 (1964).
5. Zucker, UCRL-76896, (1975).
6. Sahlin, H.L., UCID-16989.
7. Lee, J.H., et al., ATOM-KERNENERGIE, 32, 76 (1978).
8. Gribkov, V.A., et al., ATOM KERNENERGIE, 36, 167 (1980).
9. Fisher, A.G., KERNTECHNIK 20, 182 (1978).
10. Kaye, R., Intern. Conf. Plasma Science (1981).
11. Cloth, P., et al., Proc. Intern. Conf. Radiation Test Facilities for CTB Surface and Material Program (1975).

12. Decker, G., et al., PHYSICA, 28, 155 (1976).
13. Lee, J.H., IEEE Intern. Conf. Plasma Science (1979).
14. Kuyel, B., SPIE Vol. 275 Semiconductor Microlithography (1981).
15. Dense Plasma Research Group, PHYSICS JOURNAL, 24, 309 (1975).
16. Wang Jia, Qinghua University Journal, 22, 3(1982).
17. Gas Discharge Laboratory, Qinghua University Science Report, 7H, 78001, (1978).
18. Maissonier, C., et al., Sixth Inter. Conf. Plasma Physics and Contr. Nucl. Fusion Research (1976).
19. Gates, D.C., BULL. AM. PHYS. SOC. II-15, 1464 (1970).
20. Bernard, A., Intern. Conf. Plasma Phys. and Contr. Fusion Research Vol II, (1978).
21. Huebner, K., 8th IEEE Inter. Conf. Plasma Science (1981).
22. Nardi, V., et al., Ibid.
23. Steinmetz, K., PLASMA BERICHET 1/80 (1980), Heidelberg Uni.
24. Bertalot, L., European Conf. Nucl. Fusion and Plasma Physics (1981).
25. Bykovsky, U.A., Ibid.
26. Decker, G., et al., PLASMA PHYS, 22, 245 (1980).
27. Decker, G., PHY. FLUIDS, 26, 571 (1983).
28. Czekaj, S., et al., 11th European Conf. Nucl. Fusion and Plasma Physics (1983).
29. Ruckler, B., IPF-81-1 Stuttgart Uni. (1981).
30. Hayed, A., et al., IPF-82-7 Stuttgart Uni. (1982).
31. Kaeppeler, H.J., IPF-83-2 Stuttgart Uni. (1982).
32. Grauf, W., IPF-82-14 Stuttgart Uni. (1982).
33. Herold, H., et al., Ninth Intern. Conf. Plasma Phys. and Contr. Fusion Research (1982).
34. Sadowski, M., 11th European Conf. Nucl. Fusion and Plasma Physics (1983).

35. Bertalot, L., et al., PHYS. LETTERS, 79A, 289(1980).
36. Mozer, A., et al., APP. PHYS., 53, 2959 (1982).
37. Yokoyama, M., Eighth Intern. Conf. Plasma Phys. and Nucl. Fusion Research, (1981).
38. Gullickson, R.L., Inter. Conf. Plasma Science (1979).
39. Rhee, M.J., APP. PHYS. LETT. 37, 906 (1980).
40. Stygar, W., NUCL. FUSION 22, 1161 (1982).

3012/9365
CSO: 4008/415

'SCREEN' EDITING PROGRAM IN CHINESE

Shenyang XIAOXING WEIXING JISUANJI XITONG [MINI-MICRO SYSTEMS] in Chinese
No 2, 8 Feb 85 pp 60-62

[Article by Mei Miaoping [2734 1181 1627] of Jiangsu Institute of Computing
Technology]

[Text] The on-screen editing program is one of the most important software packages for many microcomputers. Because it is effective and convenient to use, it is the most popular software program among programmers. A powerful on-screen editing program often contains more than 20 editing commands. These commands can be used flexibly to edit a document such as a source program. It is much more convenient to use than a text editor.

However, the microcomputer on-screen editing program is only suited for editing documents in western languages. As we modify microcomputers to accept Chinese characters, it is necessary to simultaneously consider modifying the on-screen editing program to become a Chinese on-screen editing program to satisfy the need to promote microcomputers in China. In this paper, we will introduce an existing Chinese on-screen editing program which is used in the C-10SP Chinese system on CROMEMCO, as well as on intelligent Chinese terminals. We modified the on-screen editing program SCREEN supported by CDOS to become an on-screen editing program in Chinese and managed to maintain all capabilities.

Conditions for Its Realization

1. To convert a western language on-screen editing program to a Chinese editor, it is first necessary to have the hardware support, i.e. the CRT must be able to display Chinese characters. In addition, we must be able to control the cursor, which is the basis for the realization of screen editing.

This on-screen editing program was materialized on the basis of the hardware modification of the C-10SP system. The modified C-10SP system can display 12 lines of Chinese characters at 40 characters per line. In addition, it has a fixed primary Chinese character bank and the cursor movement can be controlled. Cursor control commands include:

- * clear screen and return cursor to upper left corner (HOME).
- * move cursor to upper left corner (HOME).
- * move cursor one space to left.
- * move cursor one space to right.
- * move cursor up one line.
- * clear text from cursor position to end of line.
- * clear text from cursor position to end of line. (Translator's note: a duplicate line)
- * move cursor to specified line and column.

These are the fundamental commands to realize screen editing.

2. Chinese data format

The machine code of each Chinese character contains two bytes. The most significant digit of the first byte is 1 and that of the second byte is 0. When the most significant digit is 1, it also serves as a Chinese character label which signifies that this byte and the next byte form a Chinese word. Simultaneously, when the most significant digit of a byte is 0, if that of the previous byte is 1 then this byte is the second byte of a Chinese character. Otherwise, this is an ASCII character. The on-screen editing program must depend on this feature to distinguish a Chinese character from an [ASCII] character.

Special Feature of the Chinese Character On-Screen Editing Program

As we compare a Chinese character on-screen editing program to an [ASCII] character on-screen editing program, in addition to having similar editing capabilities, it should also possess the following special features:

1. Each Chinese character must be processed as a unit when it is inserted, deleted or modified. In other words, two bytes of machine code must be processed simultaneously for a Chinese character. Especially in deleting, we cannot delete one byte at a time. Otherwise, we may create the wrong combination. Therefore, it is necessary to identify whether it is a Chinese word or an [ASCII] character in order to treat it properly.
2. The cursor movement must also determine whether it is in a Chinese character position or an ASCII character position. (On the screen, each Chinese character occupies two ASCII character positions, and two cursor positions as well.) If it is in a Chinese character position, it must automatically be positioned in the first byte, which is the front part of the Chinese character. Thus, it is not possible to accidentally insert the text between two bytes of a Chinese character by mistake, which may also result in deleting a half of the Chinese character.

3. When searching for an [ASCII] character, it is necessary to determine whether that character is the real one we are looking for or if it is the second byte of the machine code of a Chinese character.

The Chinese on-screen editing program is practical only when the above requirements are materialized.

Modification Method

The basic structure of the SCREEN program is:

1. Due to its special features, we decided to set up various pointers to control document editing and cursor location. The pointers used in SCREEN include: document cursor pointer, buffer pointer, screen cursor pointer (row pointer and column pointer), and left and right deleting pointer.

2. Each editing command is entered from the common entrance. Through interpretation, it is switched to the corresponding subroutine to process the command, i.e. each editing command has a corresponding processing module.

3. Cursor movement, carriage return and line feed commands are common subroutines to be dispatched by each command module, as required.

Based on the above structural characteristics, the focus of modification should be placed on the command processing modules. Furthermore, we should avoid modifying pointers and cursor movement subroutines to prevent contradictions.

An analysis of the source program of SCREEN shows that there are two key subroutines among the command processing subroutines, i.e. the leftward character processing subroutine and the rightward character processing subroutine in the editing buffer. When these two subroutines are used to process characters, their primary function is to redefine the corresponding pointers. They are common subroutines required by various command modules. Let us briefly introduce the method of modification.

A simplified block diagram of these two subroutines and the modified parts (dotted line) are shown in Figure 1. From the figure we can see that the left and right character subroutines are processed by the cursor pointer. When we process Chinese characters, these subroutines are used to treat the pointers to avoid confusion. The methodology is to add the identification of Chinese characters to these two subroutines and to install Chinese character labels. The modified portion is expressed in dotted lines. If the byte treated is a Chinese character, then a Chinese label is placed. If it is an ASCII character, the Chinese character label is cleared. When these two subroutines are called for in processing an editing command, if different treatment for a Chinese and an ASCII character is required (such as moving the cursor one space to the left or right), this subroutine should be called to determine whether it is a Chinese character. If it is, then the program will be run again and the Chinese label will be removed. Thus, we can avoid modifying the operation of the pointers. Regeneration of pointers is completely carried out by these two subroutines.

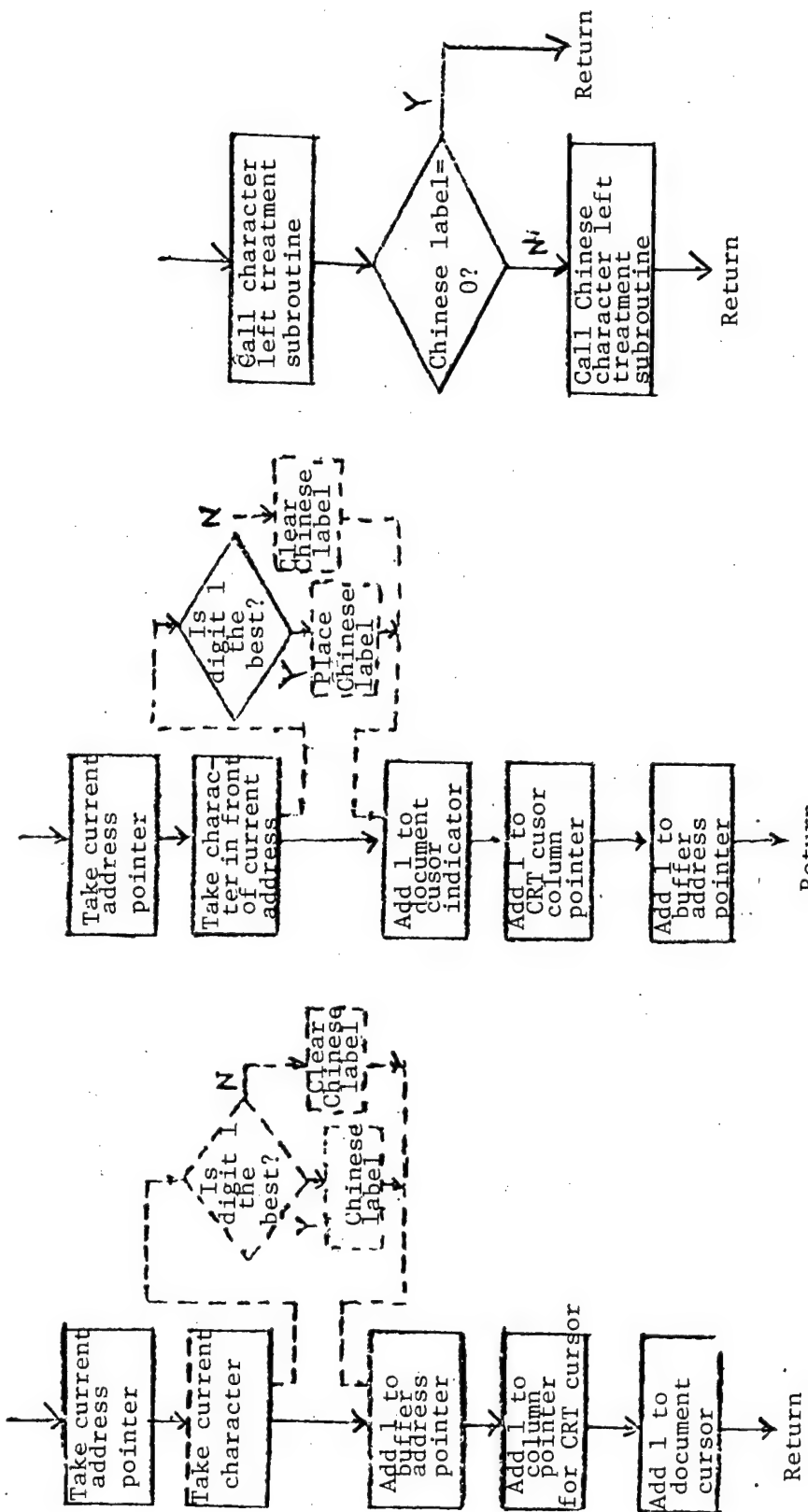


Figure 1

Figure 2 Moving Cursor
One Space Left

For instance, the modified command to move the cursor one space to the left is shown in Figure 2. We can see that when this command is issued, if the cursor is moved to the second byte of a Chinese character, it will automatically shift one more space to the left to ensure that the cursor is always located at the first byte of a Chinese character. On the screen, the cursor is always stopped at the front part of a Chinese character.

When processing Chinese characters with commands involving these two subroutines, the method to determine whether the most significant digit of the first byte is 1 is used.

We conducted specific analysis on each command module and appropriately modified them successfully based on the above method. When using this Chinese on-screen editing program to edit documents, all design specifications were met. The cursor movement differs automatically depending on whether it is a Chinese letter or a character. No confusion results from the search and replace command. Ambiguity of Chinese codes is eliminated. The program is well regarded in practice.

12553/7358
CSO: 4008/1069

SINGLE-PASS MIXED LATTICE METHOD AND CHAN-2 CODE FOR SUBCHANNEL ANALYSIS OF REACTOR

Beijing HE KEXUE YU GONGCHENG [CHINESE JOURNAL OF NUCLEAR SCIENCE AND ENGINEERING] in Chinese Vol 5 No 2, Jun 85 pp 113-119

[Article by Zhao Zhaoyi [6392 0340 7328], Zang Xinian [5258 1585 1628] of Qinghua University, and Zhou Quanfu [0719 0356 4395] and Zhao Huimin [6392 1979 2404] of 728 Research and Design Institute; manuscript received 12 March 1984]

[Abstract] In this paper the reliability and advancement of the single-pass mixed lattice method has been demonstrated. It has also been shown why CHAN-2 code is more efficient than COBRA-III C/MIT-2 code. By means of the calculation for the exit water temperature in hot assembly of Maine Yankee core the computational result which is calculated using CHAN-2 code agrees well with the measured value in the reactor. Comparison of the computational results for reactor core of Qinshan Nuclear Plant by means of subchannel analysis with those by means of single-channel analysis has also been presented.

/9365
CSO: 4009/291

OPERATING LIMIT OF WATER REACTOR PRESSURE VESSEL

Beijing KE KEXUE YU GONGCHENG [CHINESE JOURNAL OF NUCLEAR SCIENCE AND ENGINEERING] in Chinese Vol 5 No 2, Jun 85 pp 120-131

[Article by Zhang Jingcai [1728 2417 2088] of the Southwest Institute of Nuclear Reactor Engineering; manuscript received 18 January 1984]

[Abstract] The operating control principle and method for the water reactor pressure vessel, as an approach to prevent the brittle fracture of reactor coolant pressure boundary, has been described, based on the requirements of ANSI N18.2 and 10 CFR 50App.A. Calculation has been made in accordance with both the transition temperature approach and the linear elastic fracture mechanics approach. The operation limit diagram for the cylindrical shell of the pressure vessel of a 900MWe nuclear power plant is obtained.

The results obtained by different methods are analyzed and compared, and comments are given.

REFERENCES:

1. ANS-51.1/n18.2 Nuclear Safety Criteria for the Design of Stationary Pressurized Water Reactor Plants. Compilation of American Nuclear Society Standards, Vol 2, 564 (1977).
2. Title 10, Code of Federal Regulations, Part 50, Licensing of Production and Utilization Facilities, Appendix A, General Design Criteria for Nuclear Power Plants.
3. American Society of Mechanical Engineers, ASME Boiler and Pressure Vessel Code (1977), Section III Rules for Construction of Nuclear Power Plant Components, Section XI Rules for Inservice Inspection of Nuclear Reactor Coolant System.
4. Bureau of Ships, Department of the Navy, Tentative Structural Design Basis for Reactor Pressure Vessel and Directly Associated Components, PB-151987 (1958).
5. Ranganath, S., "Fracture Mechanics Evaluation of a Boiling Water Reactor Vessel Following a Postulated Loss of Coolant Accident," 5th (1979) SMIRT, G1/5.

6. Ramini, D.R., "A Fracture Mechanics Method of Evaluating Structural Integrity of a Reactor Vessel Due to Thermal Shock Effects Following LOCA Condition," 4th (1977) SMIRT, G9/4.
7. Langer, B.F., "Approximate Formulae for Calculation of Thermal Stress in Reactor Vessel, Thermal Shields and Yhimbles," WAPDCE-39 (1955).
8. Smith, L.W., "Reactor Handbook" (1964), Vol IV Engineering, Chapter 6, Structural Analysis.

/9365

CSO: 4009/291

CALCULATION OF NEUTRON FLUENCE ON PRESSURE VESSEL FOR NUCLEAR POWER STATION

Beijing HE KEXUE YU GONGCHENG [CHINESE JOURNAL OF NUCLEAR SCIENCE AND ENGINEERING] in Chinese Vol 5 No 2, Jun 85 pp 132-138

[Article by Sheng Weilan [4141 4850 5695] of the Southwest Institute of Nuclear Reactor Engineering; manuscript received 22 July 1983]

[Abstract] The neutron fluence on pressure vessel for nuclear power station is calculated, using two dimensional discrete ordinates radiation transport code DOT3.5. The results are consistent with measurement within +20 percent. The calculation sensitivity and deviation are analyzed, including various uncertainties. The total standard deviation of calculated neutron fluence is +20 percent. This is consistent with the comparison between calculation and measurement.

REFERENCES:

1. RSIC Computer Code Collection, ANISN, A One Dimensional Discrete Ordinates Transport Code.
DOT3.5, Two Dimensional Discrete Ordinates Radiation Transport Code.
TAPEMAKER, a Routine To Prepare a "Group Independent Cross Section Tape for ANISN," MESH(R-θ), MESH (R-Z) Code for Determining the DOT Fixed Neutron Source, BNL Memo. (1981)
GOFRR Generator of Graphical Output of DOT and ANISN Flux and Reaction Rates.
2. CE-18074-891, August (1980).
3. C-E Procedure 00000-FMD-401, Rev.0, November (1978).
4. CASK-40 Group Coupled Neutron and Gamma-Ray Cross Section Data, ONRL (1973).
5. Ford, W.E., III, Sanford, R.T., et al., ORNL/TM-5249, March (1976).
6. Gritzner, M.L., EPRI NP-152 (1977).
7. CASMO A Fule Assembly Burnup Program, AE-RF-76-4158, June (1978).
8. West, J.T., et al., TRANS. AM. NUCL., 28, 642 (1978).

/9365

CSO: 4009/291

GAMMA RADIATION EFFECT OF THE SYSTEMS TBP-KETONE, TBP-DMSO, AND THEIR ENERGY TRANSFER KINETICS

Beijing HE KEXUE YU GONGCHENG [CHINESE JOURNAL OF NUCLEAR SCIENCE AND ENGINEERING] in Chinese Vol 5 No 2, Jun 85 pp 139-146

[Article by Yi Min [0122 2404], Chen Dingfang [7115 1353 5364], Ha Hongfei [0761 7703 7378], and Wu Jilan [0702 1323 5695], Department of Technical Physics, Peking University; manuscript received 7 April 1984]

[Abstract] Work at this laboratory has proved that under γ -radiation TBP may form at least three kinds of active species or states in TBP-DBBP, TBP-DBPP, and TBP-DBBP-D₆H₆ systems.

In order to spread these studies, experiments were performed in TBP-Ketone and TBP-DMSO systems. $\text{>}C = 0$ and $\text{>}S = 0$ have similar bond as $\text{>}P = 0$. The displaced groups on carbon and sulphur atoms and the different polarity of those molecules will give rise to different effects on the energy transfer. The systems used are convenient to distinguish the different active species of irradiated TBP and easy to observe the sensitized process of additives.

The results show that both $\text{CH}_3\overset{0}{\underset{||}{\text{C}}}\text{CH}_3$ and $\text{CH}_3\overset{0}{\underset{||}{\text{S}}}\text{CH}_3$ have double effect of energy transfer for two kinds of excited states of TBP. So the range in energy transfer systems with TBP and the applicability of sensitized equation derived in this laboratory have been extended.

The kinetic study has also been done in this work. The inhibition equation $G_i = G_0 (1-nx)$ for the second excited state of irradiated TBP was derived, here n represents the efficiencies of energy transfer, being different for different inhibitors.

A new explanation about the inhibition equation for second excited state of TBP* was provided. The aggregations (or domains) formed by one molecule of inhibitor with several molecules of TBP should be considered to be more reasonable. In these aggregations (or domains) the energy of excited TBP* can be transferred to the molecule of inhibitor.

/9365
CSO: 4009/291

PHYSICAL START-UP OF HEAVY WATER RESEARCH REACTOR WITH UO₂ FUEL CORE

Beijing HE KEXUE YU GONGCHENG [CHINESE JOURNAL OF NUCLEAR SCIENCE AND ENGINEERING] in Chinese Vol 5 No 2, Jun 85 pp 174-180

[Abstract] Physical start-up has been performed with the UO₂ fuel core in HWRR. An on-line computer is used during the experiments. The experimental results have verified the theoretical design, and the main physical characteristics necessary to operators and users have been provided. The relationship between the height of the control rod bank and excess reactivity was studied and explained. A practical and convenient method for the excess reactivity measurement during the core life-time was given.

/9365

CSO: 4009/291

END